

# Quasars behind the disk of M 31 galaxy

P. Nedialkov<sup>1</sup>, B.F. Williams<sup>2</sup>, V.D. Ivanov<sup>3</sup>, A. Valcheva<sup>1</sup>, Y. Solovyeva<sup>4</sup>, A. Vinokurov<sup>4</sup>, E. Malygin<sup>4</sup>, D. Oparin<sup>4</sup> and O. Sholukhova<sup>4</sup>

<sup>1</sup> Department of Astronomy, Faculty of Physics, Sofia University “St. Kliment Ohridski”, 5 J. Bourchier blvd, Sofia 1164, Bulgaria  
e-mail: japed@phys.uni-sofia.bg

<sup>2</sup> Department of Astronomy, Box 351580, University of Washington, Seattle, WA 98195, USA

<sup>3</sup> European Southern Observatory, Karl-Schwarzschild-Str. 2, D-85748 Garching bei München, Germany

<sup>4</sup> Special Astrophysical Observatory, Nizhny Arkhyz 369167, Russia

Accepted Feb 16, 2026

## ABSTRACT

**Aims.** We aim to increase the limited number of quasars behind M 31, necessary for probing the chemical content of the gas and for proper motion reference, with reliable and homogeneous redshift measurements from emission lines.

**Methods.** We carried out spectroscopic follow up of 32 quasar candidates.

**Results.** We confirm 23 quasars: two are new discoveries (J004029.727+403705.68 and J004215.489+412031.52) and the rest were reported elsewhere, but with somewhat deficient analysis; 16 spectra are published for the first time. We report new homogeneous redshifts for 34 quasars (from 40 spectra, adding 17 from archives) and summarize all available information about bona-fide quasars with reliable redshift, bringing their number to 124 within the  $\mu_B=26^m/\square''$  isophote. We carried out a comparison of redshifts from different sources and excluded some objects with redshifts derived from low-resolution spectra. We derive the reddening for them from the color excess with respect to dereddened counterparts with similar redshifts in the field. Comparisons of our reddenings with M 31 reddening maps found no significant correlations.

**Conclusions.** Most QSOs behind M 31 show low reddening and do not probe high-extinctions underlining the need to identify fainter quasars behind nearby galaxies, especially behind higher extinction regions – probably due to a bias towards following up brighter and less extinct candidates. Finally, the redshifts derived from low-resolution spectra must be treated with caution, because they can contain significant errors.

**Key words.** quasars: general – quasars: emission lines – quasars: absorption lines – Line: profiles – Techniques: spectroscopic – Galaxies: distances and redshifts

## 1. Introduction

Quasars behind nearby galaxies are of great value for probing their kinematics and interstellar medium. They establish a non-moving reference system for astrometric studies (Kallivayalil, van der Marel, & Alcock 2006; Kallivayalil et al. 2013; van der Marel et al. 2019). The quasars are background sources that allow to study the extinction in the intervening absorbers that can be both nearby low-redshift galaxies or distant high-redshift objects (Crampton et al. 1997; York et al. 2006; Meusinger et al. 2010). The imprinted narrow absorption features from the interstellar material (ISM) on the quasar spectra can be used to measure the chemical composition and the velocity field of the ISM (e.g., Srianand et al. 2013; Fox et al. 2013; Richter et al. 2013; Fox et al. 2014; Combes et al. 2021). These observations, carried out in the UV, where the strong absorption features of the cold interstellar gas are, allow to trace the chemical enrichment history of the intervening galaxies, and to trace the origin of the extended gaseous structures, such as the Magellanic stream, to a particular galaxy, in this case – to the Small Magellanic cloud. UV bright quasars are necessary for such studies and they are usually found from surveys in the region such as GALEX (e.g., Worseck & Prochaska 2011), but they are relatively rare and only a few exist behind the nearest galaxies.

The mere identification of quasars is a challenge on its own. Usually, it is based on their optical colors (Peters et al. 2015), variability properties (Giveon et al. 1999; Chen et al. 2020), or their X-ray, UV or mid-infrared (mid-IR) emission (Chartas, Kulkarni, & Asper 2013; Morishita 2021; Guo et al. 2018, among others). The presence of a galaxy in front of the quasar introduces additional complications – contamination from foreground sources that in the general case can be variable, e.g. seeing dependent or due to the intrinsic variability of the contaminating source. However, these problems are solvable, for example, with a combination of some of these methods: Cioni et al. (2013) and Ivanov et al. (2016, 2024) easily reached a success rate of >70% despite the contamination from the Magellanic clouds, selecting quasar candidates from near-infrared (near-IR) colors and variability. They defined a locus of previously known quasars on the  $J-K_S$  vs  $Y-J$  color-color diagram with photometry from the VISTA Magellanic Survey (VMC; Cioni et al. 2011) and followed up spectroscopically objects located inside this region. Its borders were adjusted to reduce the contamination, mostly from evolved stars. This is acceptable as long as the goal of the search is to efficiently identify quasars, but not necessarily to obtain a complete sample. Next, they took advantage of the time-series data from the VMC survey to identify the most variable objects by parameterizing the light curves with a simple linear fit and required a minimum absolute slope value.

M31 and M33 present a greater challenge than the Magellanic system due to the higher surface stellar density, the worse contamination by objects in the more crowded intervening galaxies and because of the generally higher extinction, except for the inner SMC region.

Here we report the confirmation of 23 quasar candidates behind the M31 disk with spectra (resolution  $700 \leq \lambda/\Delta\lambda \leq 1100$ ). Two of them are completely new discoveries, and the other 21 spectra confirm the quasar nature of previously announced candidates. We also uniformly measured redshifts for 34 unique quasars from 40 spectra – adding 17 archival to our data. Summarizing, we built a list of 125 spectroscopically confirmed QSOs within the  $\mu_B=26^m/\square''$  isophote (Sec. 2).

The next two sections describe our target selection and the observations. Section 4 presents the analysis of the spectra, Section 5 is an extinction study and 6 gives a summary.

## 2. Target selection

M31 and M33 present a greater challenge than the Magellanic clouds due to the higher surface stellar density. The census of the quasars behind any galactic disk depends on its adopted boundaries. For example, Massey, Neugent, & Levesque (2019) list 8 previously known and 7 newly found QSOs<sup>1</sup> within the footprint of M31 Local Group Galaxy Survey (LGSS; Massey, Neugent, & Smart 2016). Three more QSO, known at the time, were missing in this list: one reported by Huo et al. (2013) and two others – by Liao et al. (2019), bringing the total number of the known QSOs within this survey up to 18.

However, the LGSS is designed to cover the region of active star formation, especially the eastern side that is further from the Milky Way; the M31's disk extends further outside the survey's footprint. To compensate for this offset, we adopt here a wider and physically defined area of interest adopting as a galaxy limit the ellipse with a major diameter  $D_{26}=225'$ , corresponding to the surface brightness level  $\mu_B=26^m/\square''$  of Walterbos & Kennicutt (1987). We adopt a position angle  $PA=35$  deg and major-to-minor diameters ratio of 3.09 that RC3 (Third Reference Catalog of Bright Galaxies; de Vaucouleurs et al. 1991) reports for the somewhat brighter, but better defined standard isophote of  $\mu_B=25^m/\square''$ . For the center of M31, we adopt the coordinates as determined in 2MASS (Skrutskie et al. 2006):  $\alpha=0:42:44.33$   $\delta=+41:16:07.5$  (J2000).

Our ellipse encompasses well all footprints of the modern catalogs with IR and optical photometry in M31, as well as the dust maps available in the literature.

We found spectra of 6 candidates, in addition to the previously known 18 quasars within the selected area. Four of these extra spectra were observed by LAMOST (Large Sky Area Multi-Object Fibre Spectroscopic Telescope) as a part of its Quasar Survey 2012-2017 (Dong et al. 2018; Liao et al. 2019) and are publicly available in LAMOST DR5<sup>2</sup>. Other 2 QSOs are reported by Huo et al. (2013). Interestingly, the latest LAMOST Quasar Survey DR6-DR9 2017-2021 (Jin et al. 2023) does not report any QSOs behind the M31 disk.

In total, there are 25 objects with spectroscopically derived optical redshifts within the D26 ellipse: 24 bona-fide QSOs with prominent emission lines and a BL Lac discovered

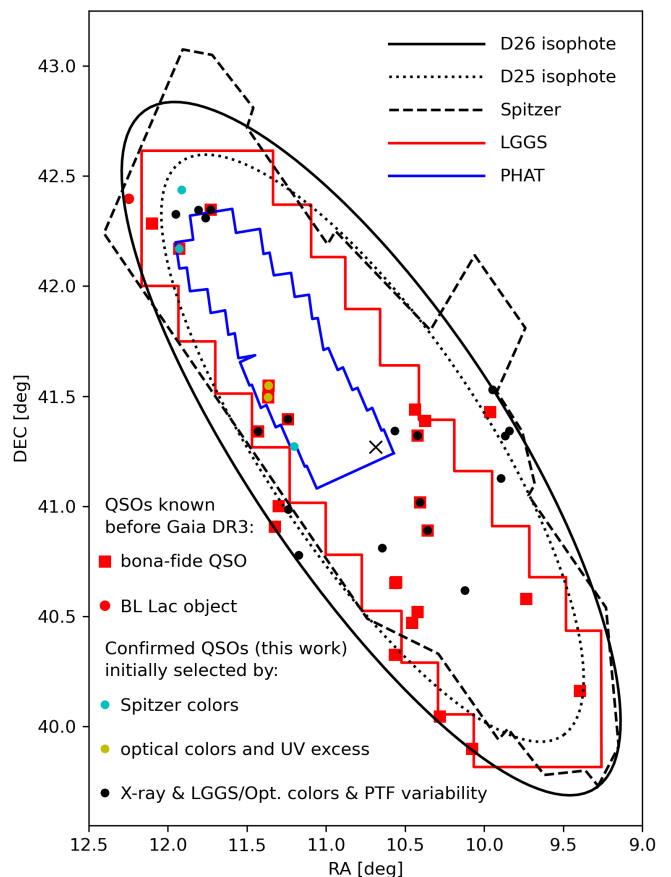


Fig. 1: Map of the 24 bona-fide QSOs (red squares) with prominent emission lines and 1 BL Lac object (red dot) known from the literature before Gaia DR3 (Gaia Collaboration et al. 2023b). The confirmed QSOs from our target list are also shown: 3 *Spitzer*-selected (cyan), 2 selected from optical colors and UV excess (yellow) and 18 selected by other means (see Table 1; black). All objects are located within the  $\mu_B=26^m/\square''$  isophote (black solid line). The  $\mu_B=25^m/\square''$  isophote (dotted line), the approximate boundaries of the *Spitzer* PSC catalog (dashed line) and the footprints of LGGS (red) and PHAT (blue) catalogs are also plotted.

by Paiano et al. (2017). Their positions are shown in Fig. 1, together with D26 and D25 isophotes and the footprints of M31 photometric catalogs: Massey, Neugent, & Smart (2016), Williams et al. (PHAT; 2014) and Khan (*Spitzer* PSC; 2017).

Recently, Gaia DR3 contributed to the global census of QSOs adding 6.4 million sources classified as AGN (Delchambre et al. 2023). The extragalactic catalog of Gaia DR3 (Gaia Collaboration et al. 2023b) reports parameters derived from various post-processing modules dedicated to the classification and characterization of more than 6.64 million objects considered as QSO candidates but only 159 quasar candidates behind the M31 disk are classified as AGN. Among them 120 have derived redshifts based on the spacecraft's spectrograph with a resolving power  $R \sim 30-100$ . However, a careful comparison with better quality data from the literature, including our own measurements reported here, suggested that about 30% of these redshifts are significantly different from measurements that we deem more reliable. This broadly agrees with their own assessment that  $\sim 36\%$  of the quasars have redshift errors

<sup>1</sup> Here, we use quasar, QSO and AGN interchangeably, because determining the exact energetics of each object is beyond the scope of this work. Furthermore, the observed broad emission lines indicate that our sample is dominated by Type 1 QSOs.

<sup>2</sup> <http://dr5.lamost.org/v3/sas/fits/>

>0.1 dex, and of Quiaa survey<sup>3</sup> that finds an even higher fraction of ~47% (if the warning flags are ignored). Therefore, we omitted from our analysis these Gaia redshifts. Objects included in this list are still considered, if other sources reported redshifts, and those other redshifts were used.

Dey et al. (2023) listed 184 “quasars behind the disk of M 31” from spectroscopy with Dark Energy Spectroscopic Instrument (DESI; DESI Collaboration et al. 2024) but only 14 of them are located within D26 ellipse. They are by-product of comprehensive spectral survey (resolution  $2000 \leq \lambda/\Delta\lambda \leq 5500$ ) of 11,416 objects on the Mayall 4m telescope at KPNO in two fields with 3'2 diameter, one centered on M 31 itself and the other to the South of it. The selection criteria involve negligible parallaxes and proper motions and combine Gaia DR2 and *unWISE* photometry (Lang 2014; Schlafly et al. 2019). They do not list errors but 51 of their quasars—many located far outside the disk of M 31—have redshifts in Barkhouse & Hall (2001), Neugent, Massey, & Georgy (2012), Huo et al. (2013), Dong et al. (2018), Massey, Neugent, & Levesque (2019), and Liao et al. (2019). Their object No. 141 with  $z=1.778$  is classified based on the LAMOST spectrum as a star at the velocity of M 31, and for their object No. 39 the LAMOST redshift is 1.600, as opposed to their 2.956; for the remaining objects the mean redshift difference is  $0.004 \pm 0.016$  and we consider this a reliable source of confirmed quasars.

Storey-Fisher et al. (2024) revisited the Gaia spectra, also combining them with *unWISE* colors. They implemented cuts based on proper motions and colors, thereby reducing the number of contaminants by approximately fourfold. They used machine learning to improve the Gaia redshift estimates. Although based on the same low-resolution Gaia spectra, the number of catastrophic outliers were reduced by a factor of 3 with respect to the unvetted analysis; 91% of their redshifts agree with the SDSS DR16 measurements (Lyke, et al 2020) to within 0.2 dex. The final catalog contains 1,295,502 quasars with  $G < 20.5$  mag, and 755,850 candidate objects in an even cleaner  $G < 20.0$  mag sample. They reported 105 QSOs within the M 31 disk. Their counterparts in Gaia DR3 which have a Class AGN are 54 and the remaining 50 are not classified.

Our data and the literature reports produce a sample of 124 unique bona-fide spectroscopically confirmed quasars and 1 BL Lac within the  $\mu_B = 26^m/\square''$  isophote.

The sample selection is heterogeneous, because of the non-uniform coverage of different surveys that provided the photometric data. Therefore, it is difficult to estimate the selection bias and completeness of our search (see Sect. 4.2).

Thirteen spectra came from a campaign to confirm optical and X-ray selected high mass binaries in M 31 (Williams et al. 2014); 12 of them were identified as quasars and one was a M star (No. 14 in Table 1).

Next, we expanded our search to the mid-IR. Initially, its footprint was limited to the Panchromatic Hubble Andromeda Treasury survey (PHAT; Williams et al. 2014) where deep and high angular resolution imaging allowed to identify isolated bright candidates that meet the mid-IR criteria of Mateos et al. (2012), based on colors from the *Wide-field Infrared Survey Explorer* (WISE; Wright et al. 2010). This is shown in Fig. 2 (top panel). We obtained spectra of 4 candidates from this selection.

We further expanded the target selection to include the Local Group Galaxy survey (LGGs; Massey, Neugent, & Smart 2016) combining it with mid-IR *Spitzer* photometry of Khan (2017). Following Mateos et al. (2012), we defined a locus (Fig. 2, mid-

dle) of known quasars in the *Spitzer* colors space as follows:

$$\begin{aligned} ([3.6] - [4.5]) &\geq -3.17 \times ([4.5] - [8.0]) + 4.75 \\ ([3.6] - [4.5]) &\geq 0.6 \times ([4.5] - [8.0]) - 0.90 \\ ([3.6] - [4.5]) &\leq 0.6 \times ([4.5] - [8.0]) - 0.05 \end{aligned} \quad (1)$$

This is an intentionally conservative definition that excludes some known quasars, but it helps to reduce the contamination by red stars. In addition, we required that  $([4.5] - [24]) \geq 4.5$  mag and that the sources are isolated – the degree of crowding index defined by Massey, Neugent, & Smart (2016) is  $< 5\%$ . Nineteen (~85%) of the 22 known quasars fall within the locus defined by these criteria; the three remaining sources are nearby AGNs where the nuclei may be contaminated by the emission from the galaxy disks (Fig. 2, bottom). Even these conservative criteria yielded hundreds of potential QSOs, but only a handful of them were bright enough in the optical for follow up spectroscopy: 10 have  $R \leq 19.2$  mag, 32 with  $19.2 < R \leq 20.0$  mag, and 62 with  $20.0 < R \leq 20.5$  mag, giving us in total 104 LGGs objects within a searching radius of 1.5". We obtained spectra of only 8 of these.

Seven quasars from Yuhan Yao<sup>4</sup> were reidentified among known X-ray (Flesch 2015) and reobserved producing homogeneous redshifts for 6 of them. The remaining object (No. 4 in Table 1) was classified as an X-ray binary.

The complete list of 32 observed candidates is given in Table 1. In the process of matching the optical and mid-IR surveys, we discovered some systematic differences in the coordinates of Khan (2017). The applied corrections with respect to WISE catalog are described in Appendix C.

### 3. Observations and data reduction

The spectroscopic confirmation was obtained by low-resolution optical spectroscopy that allows to recognize quasars from the broad emission lines in their spectra. Part of the spectra were obtained with the Dual Imaging Spectrograph<sup>5</sup> (DIS) at the 3.5m telescope at the Apache Point Observatory (marked with A in column Telescope in Table 1), with the B400 and R300 gratings in the blue ( $\lambda \approx 3425\text{--}5900 \text{ \AA}$ ) and red ( $\lambda \approx 5180\text{--}9860 \text{ \AA}$ ) channel, respectively. The 1.5 arcsec slit was used, delivering resolving power of  $R \approx 700$  and 850 at the centers of the wavelength ranges for the blue and red arms, respectively.

The remaining spectra were obtained at the 6m telescope at the Special Astrophysical Observatory (SAO) of the Russian Academy of Sciences (marked with B in column Telescope in Table 1) with SCORPIO-1<sup>6</sup> (grisms VPHG1200B and VPHG1200R, spectral ranges and resolutions are  $\lambda \approx 3600\text{--}5400 \text{ \AA}$  and  $R \approx 800$ ,  $\lambda \approx 5700\text{--}7400 \text{ \AA}$   $R \approx 1300$ , respectively; 1.2 arcsec wide slit; Afanasiev & Moiseev 2005) and SCORPIO-2<sup>7</sup> (grism VPHG1200@540, spectral range  $\lambda \approx 3650\text{--}7250 \text{ \AA}$ , resolution  $R \approx 1000$ ; 1.0 arcsec wide slit; Afanasiev & Moiseev 2011). Table 1 shows the log of our observations.

The data were reduced with Image Reduction and Analysis Facility<sup>8</sup> (IRAF; Tody 1993, 1986) and ESO Munich Image

<sup>4</sup> <https://speakerdeck.com/yaoyuhan/quasars-behind-m31-from-ptf-survey>

<sup>5</sup> <https://www.apo.nmsu.edu/arc35m/Instruments/DIS/>

<sup>6</sup> <https://www.sao.ru/hq/lsvfo/devices/scorpio/scorpio.html>

<sup>7</sup> <https://www.sao.ru/hq/lsvfo/devices/scorpio-2/index.html>

<sup>8</sup> IRAF is distributed by the National Optical Astronomy Observatory, which is operated by the Association of Universities for Research in Astronomy under a cooperative agreement with the National Science Foundation.

<sup>3</sup> <https://zenodo.org/records/10403370>

Table 1: Observing log. The columns contain: target identification, position, Gaia G band magnitude, telescope (A – Apache Point 3.5m, B – BTA 6m), UT at the start of the first exposure, number and integration time for the individual exposures (occasionally, the last exposure is shorter because the observations had to be interrupted due to poor weather and there may be a different number of exposures for the blue B and the red R channels), cross-identification with Table 2, selection criteria and comments. The astrometry and photometry is from Gaia DR3 (Gaia Collaboration et al. 2023a,b), except for the object No. 5, marked with “a”; for it the data are from Pan-STARRS Survey DR1 (Chambers et al. 2016). Asterisks indicate 16 quasars whose spectra are published for the first time.

No	Gaia EDR3	RA DEC (J2000)	G, mag	Tel.	UT start 20yy-mm-dd Thh:mm	N <sub>exp</sub> × int. time, s	No. in Table 2	Selection criteria; comments
1*	381231021002898048	00:39:21.921 41:20:31.31	20.52	B	21-11-03T21:18	6×900	15	Opt. colors & <i>PTF</i> variability
2*	381230200663395712	00:39:28.105 41:19:13.09	20.77	B	21-11-03T23:04	4×900	16	Opt. colors & <i>PTF</i> variability
3*	381223637953333376	00:39:34.595 41:07:38.52	19.88	B	21-11-04T19:34	3×900	18	Opt. colors & <i>PTF</i> variability
4*	381251297542795904	00:39:47.423 41:31:47.53	20.31	B	21-10-12T17:17	3×900	21	Opt. colors & <i>PTF</i> variability
5	156600101021498792 <sup>a</sup>	00:40:24.514 40:30:25.12	20.00 <sup>a</sup>	B	21-12-12T20:37	8×600		Opt. colors & <i>PTF</i> variability; not QSO, X-ray binary?
6*	381129011231416704	00:40:29.727 40:37:05.68	18.98	A	07-11-03T01:34	3×2700	27	X-ray & <i>LGGS</i>
				A	07-11-09T02:07	3×2700		
7	381159003004920192	00:40:45.721 40:51:34.18	19.24	A	20-01-02T04:55	2×1800		<i>Spitzer</i> colors & <i>LGGS</i> ; too low S/N to interpret
8	381161584267072896	00:41:26.217 40:53:26.55	19.95	A	07-10-10T04:38	3×2700	41	X-ray & <i>LGGS</i>
9	381164710999391104	00:41:37.918 41:01:07.82	19.40	A	07-08-10T08:55	4×1800	45	X-ray & <i>LGGS</i>
10	381276410213544064	00:41:41.408 41:19:16.85	18.57	A	07-10-09T02:05	3×2700	46	X-ray & <i>LGGS</i>
11*	381266244030810880	00:42:15.487 41:20:31.52	20.54	A	10-10-30T02:46	6×2700	57	X-ray & <i>LGGS</i>
12*	369148728241389056	00:42:35.002 40:48:39.20	18.81	A	07-08-11T10:55	3×1200	62	X-ray & <i>LGGS</i>
				A	10-10-30T01:34	3×1500		
13	369257652908605824	00:43:12.746 41:16:25.49	18.58	A	18-10-07T02:27	2×1800		UV excess in <i>LGGS</i> & <i>PHAT</i> ; not QSO, star forming region or galaxy?
14	369255522604831232	00:43:53.335 41:16:55.90	19.51	A	07-08-08T07:59	2×1800		X-ray & <i>LGGS</i> ; not QSO, early M star
15	369286102772174208	00:44:10.843 41:33:01.15	19.22	A	19-01-08T05:16	2×1500,		<i>Spitzer</i> colors & <i>LGGS</i> ; flat feature-
				A		1×602		less spectrum
16	369281288111420288	00:44:28.716 41:25:45.62	18.96	A	19-01-06T04:03	2×1500,		<i>Spitzer</i> colors & <i>LGGS</i> ; not quasar,
				A		1×1034		K-type star or globular cluster, at the redshift of M31
				A	19-01-08T04:17	2×1200		
				A	19-09-05T08:25	3×1500		
				B	22-10-25T17:33	3×900 B		
				B	22-10-25T18:25	2×900 R		
17	369281086247278080	00:44:31.624 41:24:10.69	19.86	A	19-10-27T03:35	6×1800		<i>Spitzer</i> colors & <i>LGGS</i> ; not quasar, wide emission lines object
18*	369185428738695808	00:44:41.590 40:46:43.46	19.10	B	21-10-02T22:11	3×900 B	79	Opt. colors & <i>PTF</i> variability
				B	21-10-02T22:59	2×900 R		
19	381304653920639488	00:44:45.117 41:47:20.52	19.31	A	19-10-27T01:13	4×1800		<i>Spitzer</i> colors + <i>LGGS</i> ; too low S/N to interpret
20*	369267681654714112	00:44:48.307 41:16:18.23	18.43	A	19-01-06T01:57	3×900	82	<i>Spitzer</i> colors + <i>LGGS</i>
				A	20-01-02T01:57	2×1800		
21*	369189547608980224	00:44:57.601 40:59:13.85	20.47	B	21-12-11T15:20	4×600	83	Opt. colors & <i>PTF</i> variability
22*	369268712447126272	00:44:57.938 41:23:43.72	19.67	A	07-11-09T03:45	2×1800	84	X-ray & <i>LGGS</i>
23	369288714109887744	00:45:27.311 41:32:54.06	20.39	A	18-10-07T08:03	4×1800	92	UV excess in <i>LGGS</i> & <i>PHAT</i>
24*	369276756923364224	00:45:28.249 41:29:43.92	19.53	A	18-10-07T05:08	4×1800	93	UV excess in <i>LGGS</i> & <i>PHAT</i>
25	369270469091280000	00:45:43.426 41:20:30.86	19.27	A	07-07-16T08:29	3×1800 B	95	X-ray & <i>LGGS</i>
				A		4×1500 R		
26	375332454650675328	00:46:32.809 42:13:14.25	19.10	A	18-10-07T04:06	3×900		UV excess in <i>LGGS</i> & <i>PHAT</i> ; featureless spectra, no emission lines
27	375328709439174400	00:46:55.515 42:20:50.09	17.65	A	10-10-30T05:12	3×900	108	X-ray & <i>LGGS</i>
28*	375328395906539392	00:47:02.870 42:18:37.19	19.90	A	10-10-10T07:37	8×836	109	X-ray & <i>LGGS</i>
29*	375328876942905472	00:47:13.476 42:20:47.66	19.92	A	07-07-24T08:05	4×1800	111	X-ray & <i>LGGS</i>
30*	375423881617811328	00:47:39.120 42:26:17.76	18.20	A	19-01-06T02:54	3×1200	115	<i>Spitzer</i> colors & <i>LGGS</i>
31	375322314232658048	00:47:42.847 42:10:16.93	19.74	A	08-10-26T01:29	3×2700	116	X-ray & <i>LGGS</i>
32*	375418590218050304	00:47:48.323 42:19:34.31	19.13	A	19-01-08T03:07	3×1200	118	<i>Spitzer</i> colors & <i>LGGS</i>
				A	20-01-02T03:10	3×1800		

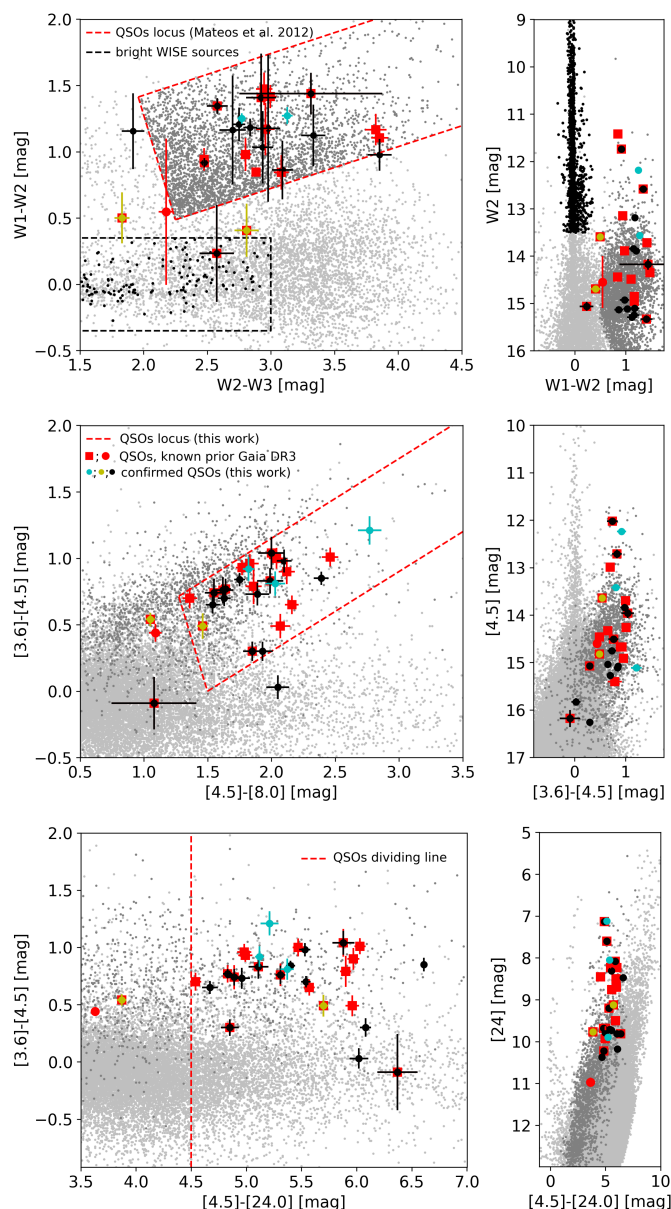


Fig. 2: Illustration of our MIR color selection (see Sec. 2 for details). *Top*: *WISE* color-color (left) and color-magnitude diagram (right). The symbols in all panels are the same as in Fig. 1. Small gray dots show the entire *WISE* photometry within the *Spitzer* footprint. Small black solid dots are the sample of bright *WISE* sources used to adjust the coordinates (see Appx. C for details). The red dashed lines show our adopted quasar locus defined in Eqs. 1 after Mateos et al. (2012). The sources falling inside are plotted with dark gray in all panels. *Middle and bottom*: Similar diagrams, but with *Spitzer* 3.6, 4.6 and 8 or 24  $\mu\text{m}$  bands. The dashed vertical line in the bottom plot shows our additional color constraint. Summarizing, our targets for follow up spectroscopy were selected among dark gray points that meet this additional criterion.

Data Analysis System<sup>9</sup> (MIDAS; Banse et al. 1988; Warmels 1992). The usual steps for long slit data processing were performed: bias/dark subtraction, flat fielding and wavelength calibration. The 1-dimensional spectra were extracted within 0.8–1.2 arcsec wide apertures, approximately matching the seeing during the observations for the DIS data, or using the optimal extraction code SPEXTRA, specifically designed for crowded fields (Sarkisyan et al. 2017), for the SCORPIO data. The spectra were flux calibrated with spectrophotometric standards from Oke (1990) and Hamuy et al. (1992, 1994), but given the non-photometric conditions during most of the observations, it is relative, so we only recovered the correct shape of the spectra, not their absolute flux. The quasar spectra are plotted in Fig. 3.

Broad-band *grizy* photometry for the quasars behind M 31 and in the surrounding field was obtained from Pan-STARRS Survey DR1 (Chambers et al. 2016).

#### 4. Quasar sample

The presence of broad lines in our spectra indicates that 23 (yellow, cyan and black solid dots in Fig. 1) out of the 32 observed objects are quasars; J004029.727+403705.68 and J004215.489+412031.52 (No. 6 and 11 in Table 1, respectively) are new and the rest are confirmations, although for 16 of these our spectra are the first to be published; the 9 non-quasars are stars, galaxies or their nature can not be reliably identified because of the low signal-to-noise of the spectra. Among 13 X-ray selected candidates, 12 turn out to be quasars; the UV excess in LGGS-PHAT selected 4 candidates yielded 2 quasars; the SPITZER-LGGS selected 8 candidates also yielded 3 quasars; 6 of 7 Yuhan Yao objects appear to be quasars. Analyzing 17 more archival spectra, in addition to our data, we uniformly measured redshifts for in total of 34 unique quasars based on 40 spectra in total.

The objects with measured redshift in this work together with the literature QSOs with spectroscopically derived redshift form a sample of 125 QSOs, located within M 31 isophote  $\mu_B=26^m/\square''$ . They are listed in Table 2, together with the lines used for the redshift measurements and the distances from the M 31 center. For the center of M 31, we adopted the coordinates of its extended core J004244.33+411607.5 (Skrutskie et al. 2006) located at 1.7'' from the center defined in RC3 (de Vaucouleurs et al. 1991). All distances  $\rho$  within the rectified plane of the galaxy are in fractions, normalized to  $\rho_{25}$ , which is the half of the major isophotal diameter  $D_{25}=190.5'$  measured at surface brightness level  $\mu_B=25^m/\square''$ . They are calculated, assuming position angle  $PA=35$  deg, determined as the ratio of the major-to-minor isophotal diameters  $R_{25}=3.0903$  (de Vaucouleurs et al. 1991) and taking into account an intrinsic oblateness of 0.14, typical for a Sb galaxy like M 31. Thus, the disk plane is inclined to the line of sight at 17.1 deg.

To outline the area of interest in this work, we tentatively adopted a larger major isophotal diameter of 225' as measured approximately at surface brightness level  $\mu_B=26^m/\square''$  by Waltherbos & Kennicutt (1987), the same axis ratio and PA as in RC3. Note that the Holmberg diameter of 200' (Nilson 1973) falls just between the previous two values, but axis ratio of 2.5 leads to a smaller inclination of 12.1 deg.

<sup>9</sup> <https://www.eso.org/sci/software/esomidas/>

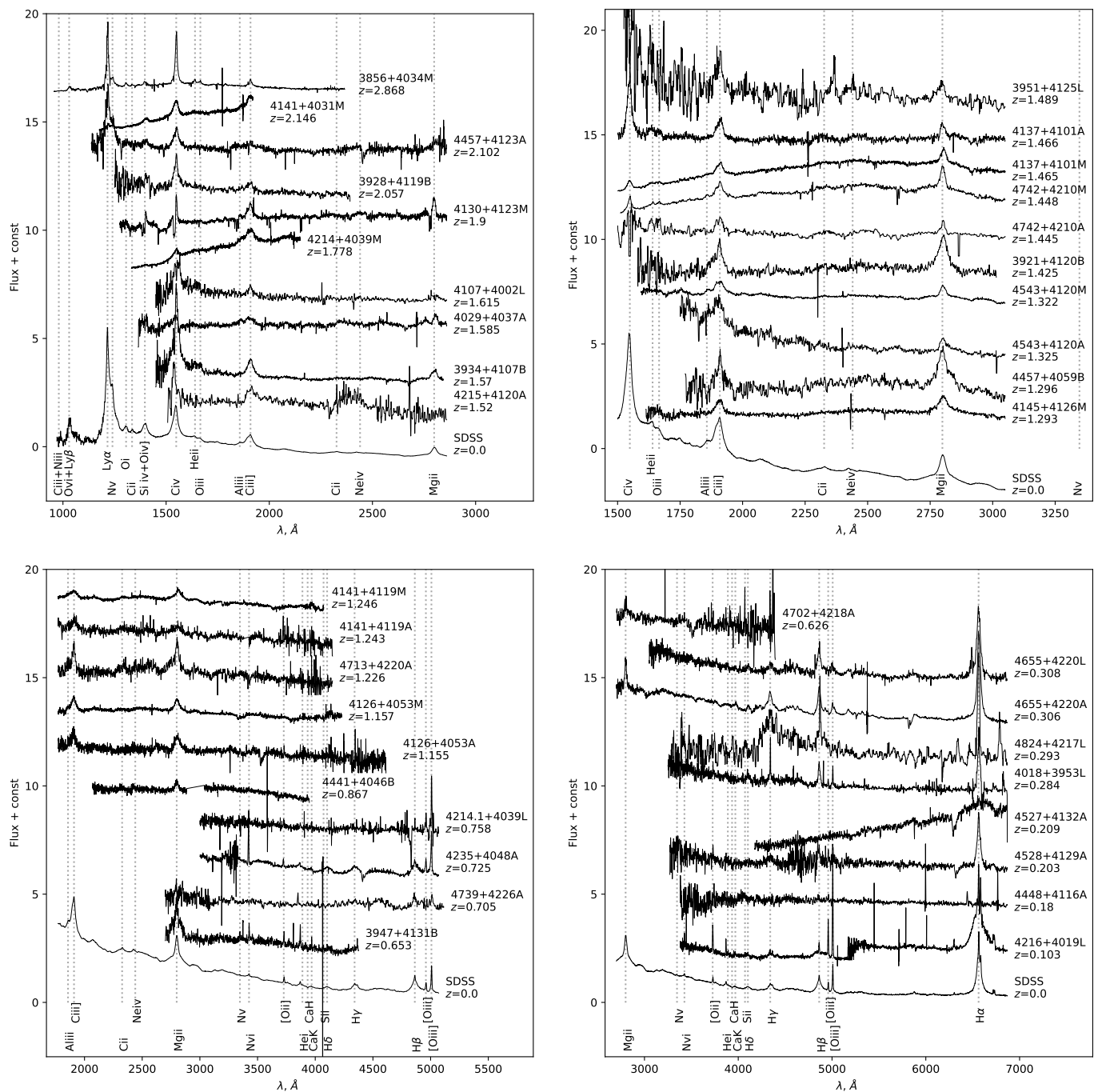


Fig. 3: Spectra of the observed objects sorted by redshift, shown at rest frame wavelength. Some more prominent features are marked with vertical dashed lines and are labeled. The SDSS composite quasar spectrum (Vanden Berk et al. 2001) is also plotted at the bottom of each panel.

#### 4.1. Redshift measurements

Quasars are easy to identify from the broad (as wide as thousands of  $\text{km s}^{-1}$ ) lines, like C $\text{IV}$  1548, C $\text{III}$  1909, M $\text{GII}$  2799 and others, emitted by the gas in the vicinity of the central supermassive black holes (BH; Bahcall et al. 1997; Peterson 1997).

We measured their redshift following closely the procedures of Ivanov et al. (2016) and Massey, Neugent, & Levesque (2019). First, we identified the broad lines comparing the spectrum of each object with the composite SDSS quasar spectrum of Vanden Berk et al. (2001). Then, we measured the observed

wavelengths of the lines fitting Gaussians to them with the IRAF task *splot* and calculated the redshift of each line. Blended lines were omitted. Lines affected by strong intervening absorption were either omitted, or if possible, Gaussians were fitted only to their cores. The final redshift of an object was determined averaging the redshifts of all emission lines. The redshift uncertainty was the r.m.s. of the individual lines' redshifts; if only two lines were available, we tentatively adopted as an error the difference between their redshifts.

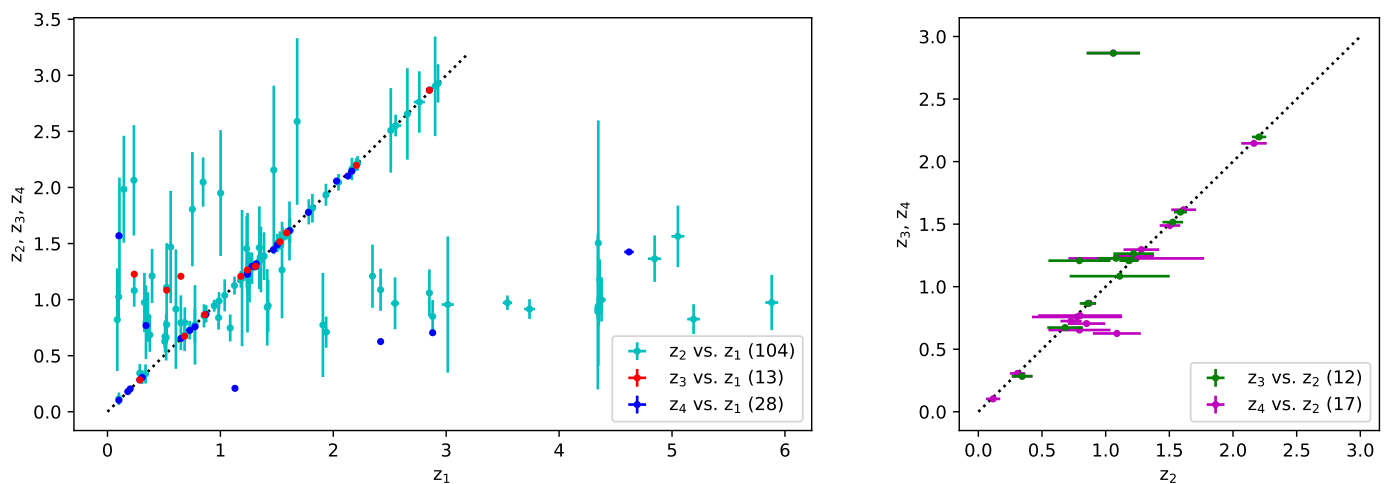


Fig. 4: Cross-comparison of redshifts from different sources:  $z_1$  – Gaia Collaboration et al. (2023a);  $z_2$  – Storey-Fisher et al. (2024);  $z_3$  – Dey et al. (2023);  $z_4$  – all other sources (listed in Table 2), including this work redshift preference when available. Left:  $z_2$ ,  $z_3$  and  $z_4$  versus  $z_1$ . Right:  $z_3$  and  $z_4$  versus  $z_2$ . The published measurement errors are shown, except for Dey et al. (2023) who do not list them – in this case for plotting purposes we adopted errors equal to 0.005 dex. The bracketed numbers in the legends show how many objects constitute the overlapping subset between each pair of samples. The black dotted line has a slope of one.

#### 4.2. Comparison with literature redshifts

In general, our redshift measurements  $z_4$  shown with dots in Fig. 4 (right), agree well with the literature, with a few exceptions. For example, we measured  $z=0.626\pm0.011$  for Gaia DR3 375328395906539392 (Nos. 28 in Table 1 and 109 in Table 2), while Gaia Collaboration et al. (2023a) and Storey-Fisher et al. (2024) reported the vastly different  $z=2.419\pm0.016$  and  $z=1.088\pm0.188$ , respectively. We identified the single emission line in its spectrum as MgII 2799, because no other prominent lines appeared within the wavelength coverage of our APO spectrum, and they should have, if the redshift was different.

For Gaia DR3 375423881617811328 (Nos. 30 in Table 1 and 115 in Table 2), we measured  $z=0.705\pm0.001$ , agreeing at  $\sim 1\sigma$  level with  $z=0.850\pm0.147$  of Storey-Fisher et al. (2024), but very different from  $z=2.880\pm0.026$  of Gaia Collaboration et al. (2023a). Our measurement is based on three lines, making the random agreement unlikely.

Gaia DR3 369288714109887744 (Nos. 23 in Table 1 and 92 in Table 2) is another case of disagreement. This is a rediscovered quasar at  $z=0.209\pm0.001$  found earlier by Dorn-Wallenstein, Levesque, & Ruan (2017) at  $z\sim 0.215$ . A third measurement of  $z=1.129\pm0.008$  (Gaia Collaboration et al. 2023a) is considered unreliable.

The largest redshift discrepancy is associated with Gaia DR3 381231021002898048 (Nos. 1 in Table 1 and 15 in Table 2). Our higher quality SAO spectrum yields  $1.425\pm0.005$ , very different from  $z=4.619\pm0.042$  of Gaia Collaboration et al. (2023a). Notably, this work gives some extremely high redshifts – with respect to Storey-Fisher et al. (2024) – for other 21 quasars.

For two objects, we measured redshifts higher than the values of Gaia Collaboration et al. (2023a). For DR3 375418590218050304 (Nos. 32 in Table 1 and 118 in Table 2), they reported  $z=0.341\pm0.003$ , while we measured  $z=0.769\pm0.002$ , very similar to  $z=0.798\pm0.328$  of Storey-Fisher et al. (2024). The decisive argument for our higher redshift is the identification of MgII 2799 in the blue arm of the APO spectrograph. The two arms are calibrated independently, in effect they are two instruments.

For Gaia DR3 381223637953333376 (Nos. 3 in Table 1 and 18 in Table 2), we measured  $z=1.570\pm0.001$ . Gaia Collaboration et al. (2023a) place it at  $z=0.101\pm0.008$  – inconsistent with our excellent quality SAO spectrum that exhibits multiple emission lines.

Not surprisingly, somewhat better agreement exists between  $z_3$  (Dey et al. 2023) and  $z_2$  (Storey-Fisher et al. 2024), and between our redshifts  $z_3$  and  $z_2$  (Storey-Fisher et al. 2024) as seen in Fig. 4, right. The only inconsistent case here is Gaia DR3 381137287633113216 (No. 7 in Table 2): Storey-Fisher et al. (2024) reported  $z=1.060\pm0.209$ , very different from our value of  $z=2.868\pm0.003$ . Our value agrees with three other measurements from the literature.

The blazar Gaia DR3 375378320605062144 (Paiano et al. 2017) was excluded from our redshift and reddening analyses, because of the contradicting  $z$  measurements in the literature and because it may not exhibit typical quasar colors.

Some objects were misidentified as quasars in the literature. Liao et al. (2019) reported that LAMOST\_10.952+40.80076 (Gaia DR3 369228137893480064) is a QSO at  $z=0.262$ . However, a careful inspection of the LAMOST DR5 spectrum (spec-55859-M5901\_sp04-015) revealed prominent CaT and other stellar features typical for K7-M0 stars. Another example is Gaia DR3 381200372113648128, listed as J003905.66+410456.6 in LAMOST DR2&3 (Dong et al. 2018) and LAMOST\_9.774+41.08240 in LAMOST DR4 (Liao et al. 2019). We did not find convincing confirmation of the  $z\sim 0.8$  derived in both these papers from the LAMOST spectra. Instead, we identified a broad feature corresponding to H $\alpha$  at the M31 rest frame and we suspected that it has been misinterpreted as Civ 1548 by Gaia Collaboration et al. (2023a) who reported  $z=3.190\pm0.027$ .

Our selection identified 9 more QSO candidates within the  $\mu_B=26^m/\square''$  isophote and we observed them (Nos. 5, 7, 13–17, 19, 26 in Table 1), but the spectra did not provide evidences for a quasar nature. This was the case with object No. 16, located in a prominent dust lane. Johnson et al. (2015) reported  $\sim 10\%$  probability that it is a galaxy. However, our spectrum lacks broad emission lines and shows absorptions making it a likely red star

or a globular cluster in M 31. These nine and the two LAMOST objects mentioned above were omitted from Table 2.

The heterogeneous nature of the selection and the lack of comparison quasars outside of the M 31 disk, confirmed by the same means and following the same strategy makes it difficult to estimate the completeness of this sample. The only exception, and the largest contribution to our sample – bringing in about 2/3 of the quasars – is the all-sky Quia survey. We compared the surface density of secure quasars, according to the classification of Gaia Collaboration et al. (2023a, see their Class, reproduced here in Table 2). There is an 10-30% excess of such objects inside of the  $\mu_B=26^m/\square''$  isophote, where the exact percentage depends on the adopted outside locus and magnitude limits. Therefore, it is not the incompleteness but rather the contamination that may be an issue for quasar searches, underlying the need for reliable spectroscopic confirmation like the follow up we report here.

### 4.3. Reliability of redshift measurements

To assess the reliability of heterogeneous literature redshifts, we compared the multiple measurements that are available for some sources (Fig. 4). Gaia Collaboration et al. (2023a) reported some relatively high redshift measurements that found no confirmation among other sources (pale blue dots on the left panel). Many outliers in Fig. 4 (left) have a probability  $P_{QSO}$  of being a quasar  $\sim 100\%$  questioning the reliability of  $P_{QSO}$  and the values of their redshifts. Further investigation revealed that these high redshifts are associated with objects not classified as active galaxies or all together lacking classification in Gaia Collaboration et al. (2023a, again, refer to the Class in Table 2). Therefore, the redshifts in Gaia DR3 must be treated with caution, unless the object is specifically classified as a high-probability active galaxy.

Other literature sources agreed better between themselves. For example Ivanov et al. (2024) finds good agreement between their own redshifts and the Quia measurements. However, taking the literature redshifts at face value seems risky. To ensure we use the most reliable redshifts, we adopted the following strategy: if an individual redshift measurement for an object is available, e.g. from our own spectra or from the literature, we prefer this value, because these as a rule are human-verified, as opposed to redshifts from large surveys that rely – as a rule – on automated procedures. This is largely driven by our concern about the objects with  $z>3$  of Gaia Collaboration et al. (2023a). In total 18 quasars fall into this group. Note that some of the spectra come from the literature, but we reidentified the emission lines and remeasured the redshifts.

If no individual measurements were available, we turned to survey data, in order of preferences: Dey et al. (2023), Storey-Fisher et al. (2024). These two surveys contributed 9 and 81 redshifts, respectively. This brings the total number of quasars with spectroscopic redshifts within the  $\mu_B=26^m/\square''$  isophote to 124, omitting the blazar, as discussed earlier.

## 5. M 31 disk extinction

We attempted to measure the extinction within the M 31 disk from the color excess of quasars within the  $\mu_B=26^m/\square''$  isophote with respect to the colors of quasars at similar redshift, located away from M 31, assuming that they show on average the same colors, as long as they are at the same redshift, and that the large number of quasars away from the disk will average out any intrinsic variations.

First, we correct both quasar samples for the foreground Milky Way extinction. Outside of M 31, we apply individual estimates from the map of Schlafly & Finkbeiner (2011). Within the M 31 body, the predicted  $E(B-V)$  increases inwards – due to the dust content of the galaxy itself. To alleviate this issue, we adopted for all objects inside the  $\mu_B=26^m/\square''$  isophote a constant foreground Milky Way extinction. We considered 326 Quia quasars within an elliptical annulus between one and two major-axis D26 isophotal diameters, to ensure that they are safely clear of M 31, but still in the general direction of the galaxy, minimizing any residual Milky Way extinction. Averaging the individual extinctions, we derived  $E(B-V)=0.060\pm 0.010$  mag, similar to  $E(B-V)=0.055$  mag that Schlafly & Finkbeiner (2011) report for the M 31 center and well within the range 0.035–0.105 mag that the same map enables.

Next, we derived the intrinsic colors  $(g-r)_0$ ,  $(g-i)_0$ ,  $(g-z)_0$  and  $(g-y)_0$ , at the redshift of each quasar behind M 31, as median over the dereddened colors of all quasars in the reference sample with redshift within 0.3 dex (Fig. 5). This reference sample was selected from the Quia catalog to include all quasars within 5 deg from the M 31 center (about 2600 objects in total, see Fig. 5 for the exact numbers in the individual colors), but outside the  $\mu_B=26^m/\square''$  isophote, to ensure averaging over 100's of quasars. We converted the color excesses to  $A_V$  adopting a total-to-selective extinction ratio  $R_V=3.1$  and according to the extinction law of Cardelli et al. (1989). We formed the  $A_V$  error for each quasar behind M 31 as a quadrature sum of the quasars' photometric errors and the variation of the intrinsic colors for the quasars at that redshift. We averaged the derived  $A_V$ 's from the four colors with error weighting. Some extinctions are negative because of the large intrinsic spread of quasar colors that can be seen in Fig. 5 and to lesser extend, the photometric errors. Furthermore, undetected contamination from blue foreground objects in M 31 itself may also lead to negative extinction, although we tried to exclude this by selecting isolated candidates for the follow up. No trend in the evolution of the broad band intrinsic colors of quasars as a function of redshift is seen when the sample is divided into several radial bins spanning 1.5 to 11  $\rho_{25}$ .<sup>10</sup>

We used two M 31 extinction maps to compare our estimates with. The map of Draine et al. (2014) has the SPIRE 350 resolution of 25''. It gives the dust surface density and its uncertainty in units of ( $M_\odot/kpc^2$ ). We converted these quantities into absorption  $A_V$  values according to the Draine & Li (2007) dust model. The map of Dalcanton et al. (2015) has 7'' resolution. It derives  $A_V$  using stellar photometry of red giant branch (RGB) stars from Williams et al. (PHAT; 2014) survey, enabling a direct comparison with our results. Only 114 of our quasars fall within the footprint of the former map and 14 – of the latter. No correlation is found in both cases (Fig. 6). This negative result is probably due mostly to the bias towards lower extinction that is rooted in the quasar selection and especially in the target selection for the spectroscopic confirmation: quasars located along more heavily obscured lines of sight are fainter and less likely to have spectra. This can be seen in Fig. 7 that overplots the quasars in the sample on the Draine et al. (2014) reddening map. Furthermore, with quasars we measure the extinction along a narrow line of sight, while the reddening maps average the extinction over wider bins. Last but not least, the number of quasars

<sup>10</sup> A stand-alone Python script that derives the intrinsic colors of quasars as a function of redshift from a sample of reference quasars outside M 31, and then calculates the color excesses and absorptions for individual quasars behind the M 31, is available at [https://github.com/vdivanov/Quasars\\_behind\\_M31\\_2026/](https://github.com/vdivanov/Quasars_behind_M31_2026/), together with the necessary input files.

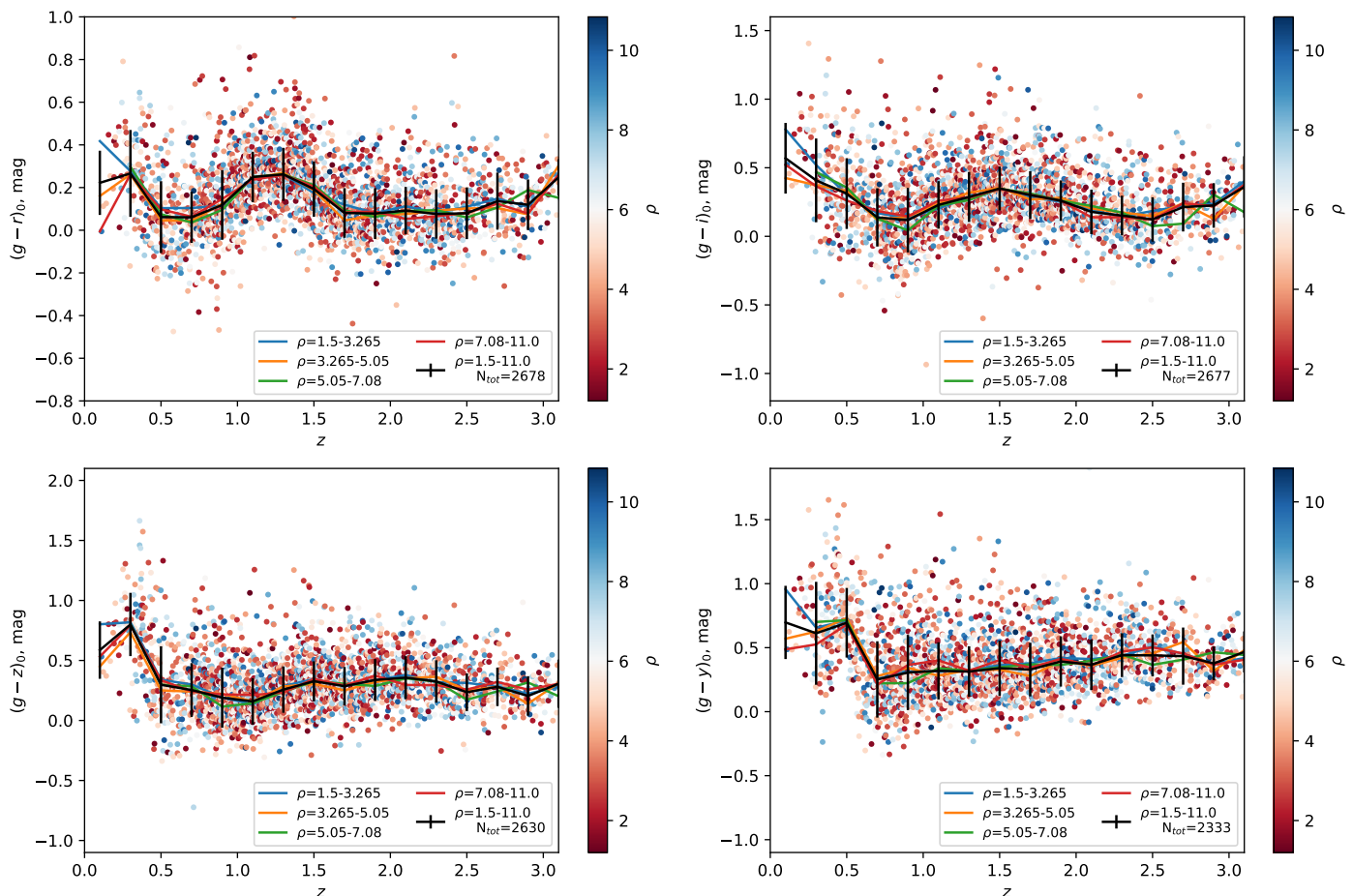


Fig. 5: Intrinsic colors of our Quiaia reference quasar sample, obtained after correcting the Pan-STARRS Survey DR1 *grizy* photometry (Chambers et al. 2016) for the Milky Way extinction according to the Schlafly & Finkbeiner (2011). The color of the points marks the distance of the quasars from the M 31 center  $\rho$  in units of  $\rho_{25}$  isophotal radii. The distance bins' widths were set to ensure these bins contain similar number of quasars. The solid lines connect the median colors within 0.5 dex wide redshift bins. The vertical error bars are the standard deviations of the colors of all quasars within each redshift bin, regardless of the distance from the M 31 center, and they were calculated as  $1.48 \times \text{MAD}$  (median absolute deviation), to suppress the influence of outliers.

may be insufficient for this test, considering the significant variation of the quasar's intrinsic colors (Fig. 5).

## 6. Summary and conclusions

We selected quasar candidates from apparent colors and X-ray emission among objects within the M 31  $\mu_B = 26^m/\square''$  isophote and carried out optical spectroscopy of the brightest of them to confirm their nature increasing the number of published spectra from 24 to 40. We also collected quasars from various public surveys, bringing the total number of bona-fide quasars behind the M 31 disk to 124 (125, counting one blazar).

Our work provides a large sample of quasars for astrometric studies of M 31 (i.e., Rusterucci et al. 2024), similar to the previous work in the Magellanic clouds (Costa et al. 2011). Quasars facilitate also studies of its interstellar medium (ISM) – both of the extinction from their colors, as we attempted to do here, and of the ISM's chemical abundances with spectroscopy, typically in the UV (Fox et al. 2013; Mishra et al. 2024). The later work will come within reach for many faint quasars with the next generation of 30-40-m class spectroscopic telescopes or with the

dedicated spectroscopic facilities, such as the WST (Wide-field Spectroscopic Telescope; Mainieri et al. 2024).

We measured the extinction inside M 31 towards 114 quasars with reliable redshifts and found no correlation with the existing reddening maps, probably because of the limited number of objects, the biases in our sample, and different physical scales of the regions that are probed with the quasars and the dust maps. This problem must be revisited when LSST helps to discover more quasars, based on their variability, as Ivanov et al. (2016, 2024) demonstrated that the variability helps to increase the efficiency of quasar selection.

Last but not least, in the course of our analysis we confirmed the previous concerns that the redshifts, derived from low-resolution spectra may contain significant errors. Such measurements must be treated with caution.

*Acknowledgements.* The authors thank an anonymous referee whose valuable comments and recommendations helped to improve the quality of the paper. PN and AV acknowledge financial support from the European Union-NextGenerationEU, through the National Recovery and Resilience Plan of the Republic of Bulgaria, project No BG-RRP-2.004-0008-C01. PN thanks Phillip Massey for sharing the spectra of 10 QSOs behind the disk of M 31 obtained with Hectospec at the MMT. PN is also grateful to Julianne Dalcanton for providing the extinction maps of the M 31 disk, based on the PHAT survey data. The search for QSOs behind the disc of the M 31 galaxy was partially sup-

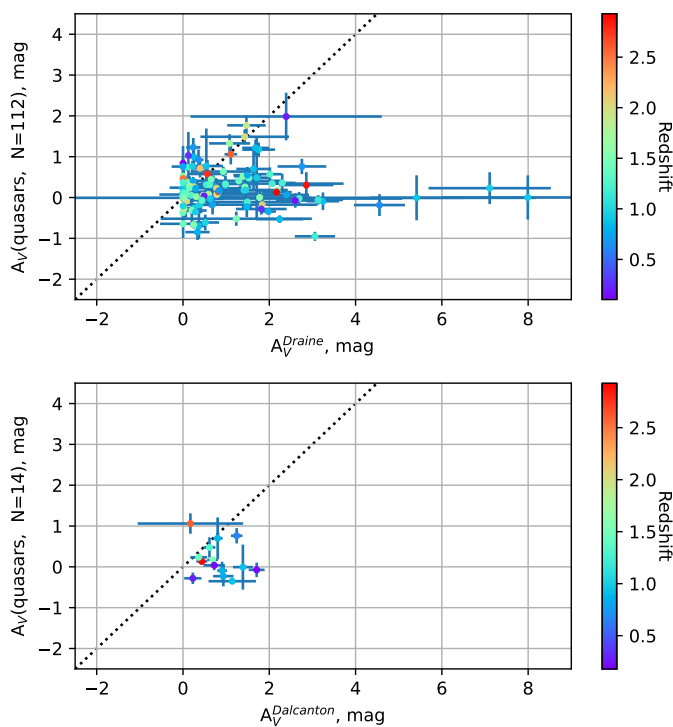


Fig. 6: Comparison of  $A_V$  derived from our quasar sample and from the reddening maps of Draine et al. (2014, top) and Dalcanton et al. (2015, bottom).

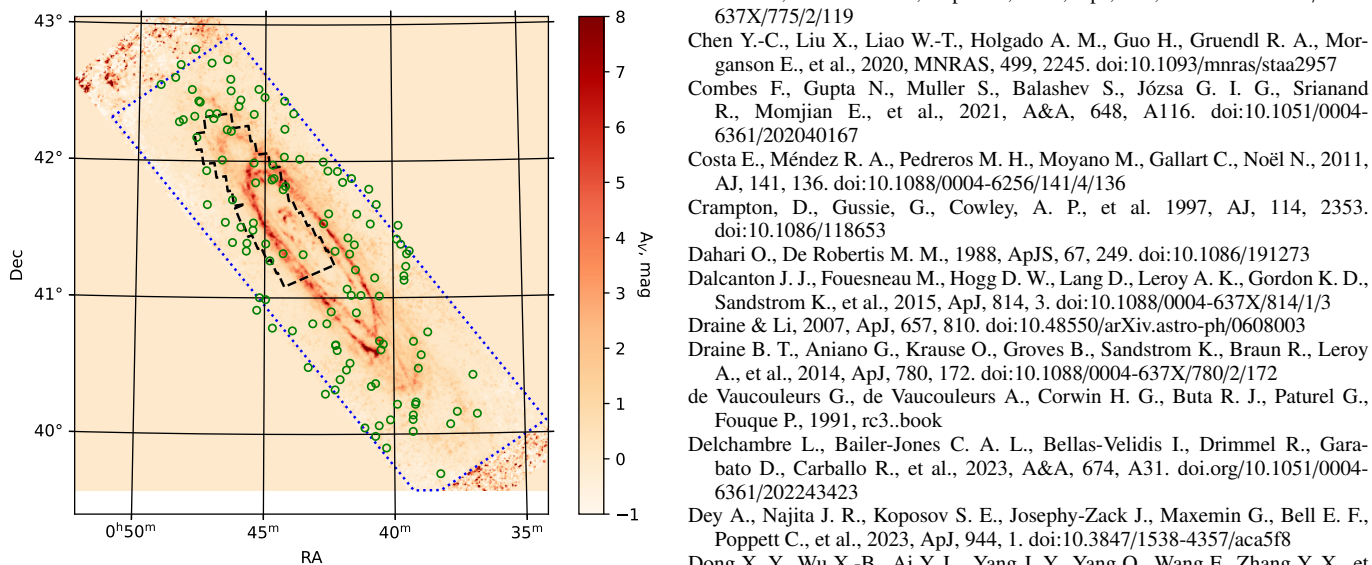


Fig. 7: Location of the quasars from our sample on the reddening maps (green open circles) of Draine et al. (2014, blue dotted line) and Dalcanton et al. (2015, black dashed line).

ported by a short-term scholar Fulbright grant of PN at the Department of Astronomy, University of Washington, for the academic year 2018–2019 from the US Department of State program number G-1-00005. This work has made use of data from the European Space Agency (ESA) mission *Gaia* (<https://www.cosmos.esa.int/gaia>), processed by the *Gaia* Data Processing and Analysis Consortium (DPAC, <https://www.cosmos.esa.int/web/gaia/dpac/consortium>). Funding for the DPAC has been provided by national institutions, in particular the institutions participating in the *Gaia* Multilateral Agreement.

Observations with the SAO RAS telescopes are supported by the Ministry of Science and Higher Education of the Russian Federation. The renovation of telescope equipment is currently provided within the national project “Science and Universities”. The BTA data reduction was performed as part of the SAO RAS government contract approved by the Ministry of Science and Higher Education of the Russian Federation. This work uses data from the Guoshoujing Telescope (the Large Sky Area Multi-Object Fiber Spectroscopic Telescope LAMOST). It is a National Major Scientific Project built by the Chinese Academy of Sciences. Funding for the project has been provided by the National Development and Reform Commission. LAMOST is operated and managed by the National Astronomical Observatories, Chinese Academy of Sciences.

## References

- DESI Collaboration, Adame A. G., Aguilar J., Ahlen S., Alam S., Aldering G., Alexander D. M., et al., 2024, *AJ*, 168, 58. doi:10.3847/1538-3881/ad3217
- Afanasyev V. L., Moiseev A. V., 2005, *AstL*, 31, 194. doi:10.1134/1.1883351
- Afanasyev V. L., Moiseev A. V., 2011, *BaltA*, 20, 363. doi:10.1515/astro-2017-0305
- Johnson L. C., Seth A. C., Dalcanton J. J., Wallace M. L., Simpson R. J., Lintott C. J., Kapadia A., et al., 2015, *ApJ*, 802, 127. doi:10.1088/0004-637X/802/2/127
- Bahcall J. N., Kirhakos S., Saxe D. H., Schneider D. P., 1997, *ApJ*, 479, 642. doi:10.1086/303926
- Barkhouse, W. A. & Hall, P. B. 2001, *AJ*, 121, 5, 2843. doi:10.1086/320377
- Banase K., Ponz D., Ounnas C., Grosbol P., Warmels R., 1988, *igbo.conf*, 431
- Cardelli, J. A., Clayton, G. C., & Mathis, J. S. 1989, *ApJ*, 345, 245. doi:10.1086/167900
- Cioni, M.-R. L., Clementini, G., Girardi, L., et al. 2011, *A&A*, 527, A116. doi:10.1051/0004-6361/201016137
- Cioni, M.-R. L., Kamath, D., Rubele, S., et al. 2013, *A&A*, 549, A29. doi:10.1051/0004-6361/201219696
- Chambers K. C., Magnier E. A., Metcalfe N., Flewelling H. A., Huber M. E., Waters C. Z., Denneau L., et al., 2016, *arXiv*, arXiv:1612.05560. doi:10.48550/arXiv.1612.05560
- Chartas G., Kulkarni V. P., Asper A., 2013, *ApJ*, 775, 119. doi:10.1088/0004-637X/775/2/119
- Chen Y.-C., Liu X., Liao W.-T., Holgado A. M., Guo H., Gruendl R. A., Morganson E., et al., 2020, *MNRAS*, 499, 2245. doi:10.1093/mnras/staa2957
- Combes F., Gupta N., Muller S., Balashev S., Józsa G. I. G., Srianand R., Momjian E., et al., 2021, *A&A*, 648, A116. doi:10.1051/0004-6361/202040167
- Costa E., Méndez R. A., Pedreros M. H., Moyano M., Gallart C., Noël N., 2011, *AJ*, 141, 136. doi:10.1088/0004-6256/141/4/136
- Crampton, D., Gussie, G., Cowley, A. P., et al. 1997, *AJ*, 114, 2353. doi:10.1086/118653
- Dahari O., De Robertis M. M., 1988, *ApJS*, 67, 249. doi:10.1086/191273
- Dalcanton J. J., Fouesneau M., Hogg D. W., Lang D., Leroy A. K., Gordon K. D., Sandstrom K., et al., 2015, *ApJ*, 814, 3. doi:10.1088/0004-637X/814/1/3
- Draine & Li, 2007, *ApJ*, 657, 810. doi:10.48550/arXiv.astro-ph/0608003
- Draine B. T., Aniano G., Krause O., Groves B., Sandstrom K., Braun R., Leroy A., et al., 2014, *ApJ*, 780, 172. doi:10.1088/0004-637X/780/2/172
- de Vaucouleurs G., de Vaucouleurs A., Corwin H. G., Buta R. J., Paturel G., Fouque P., 1991, *rc3.book*
- Delchambre L., Bailer-Jones C. A. L., Bellas-Velidis I., Drimmel R., Garabato D., Carballo R., et al., 2023, *A&A*, 674, A31. doi.org/10.1051/0004-6361/202243423
- Dey A., Najita J. R., Kuposov S. E., Josephy-Zack J., Maxemin G., Bell E. F., Poppett C., et al., 2023, *ApJ*, 944, 1. doi:10.3847/1538-4357/aca5f8
- Dong X. Y., Wu X.-B., Ai Y. L., Yang J. Y., Yang Q., Wang F., Zhang Y. X., et al., 2018, *AJ*, 155, 189. doi:10.3847/1538-3881/aab5ae
- Dorn-Wallenstein T., Levesque E. M., Ruan J. J., 2017, *ApJ*, 850, 86. doi:10.3847/1538-4357/aa9329
- Fox, A. J., Wakker, B. P., Barger, K. A., et al. 2014, *ApJ*, 787, 2, 147. doi:10.1088/0004-637X/787/2/147
- Gaia Collaboration, Vallenari A., Brown A. G. A., Prusti T., de Bruijne J. H. J., Arenou F., Babusiaux C., et al., 2023, *A&A*, 674, A1. doi:10.1051/0004-6361/202243940
- Gaia Collaboration: Bailer-Jones C.A.L., Teyssier D., Delchambre L., Ducourant C., Garabato D., Hatzidimitriou D., et al., 2023, *A&A*, 674, A41. doi.org/10.1051/0004-6361/202243232
- Giveon U., Maoz D., Kaspi S., Netzer H., Smith P. S., 1999, *MNRAS*, 306, 637. doi:10.1046/j.1365-8711.1999.02555.x
- Guo S., Qi Z., Liao S., Cao Z., Lattanzi M. G., Bucciarelli B., Tang Z., et al., 2018, *A&A*, 618, A144. doi:10.1051/0004-6361/201833135
- Flesch E. W., 2015, *PASA*, 32, e010. doi:10.1017/pasa.2015.10

- Fox A. J., Richter P., Wakker B. P., Lehner N., Howk J. C., Ben Bekhti N., Bland-Hawthorn J., et al., 2013, *ApJ*, 772, 110. doi:10.1088/0004-637X/772/2/110
- Ivanov V. D., Cioni M.-R. L., Bekki K., de Grijs R., Emerson J., Gibson B. K., Kamath D., et al., 2016, *A&A*, 588, A93. doi:10.1051/0004-6361/201527398
- Ivanov V. D., Cioni M.-R. L., Dennefeld, M., de Grijs R., Craig, J.E.M., van Loon, J. Th, Pennock, C., Maitra, Ch., Haberl, F., 2024, *A&A*, 687, A16. doi:10.1051/0004-6361/202346504
- Hamuy M., Suntzeff N. B., Heathcote S. R., Walker A. R., Gigoux P., Phillips M. M., 1994, *PASP*, 106, 566. doi:10.1086/133417
- Hamuy M., Walker A. R., Suntzeff N. B., Gigoux P., Heathcote S. R., Phillips M. M., 1992, *PASP*, 104, 533. doi:10.1086/133028
- Huo Z.-Y., Liu X.-W., Xiang M.-S., Yuan H.-B., Huang Y., Zhang H.-H., Yan L., et al., 2013, *AJ*, 145, 159. doi:10.1088/0004-6256/145/6/159
- Jin J.-J., Wu X.-B., Fu Y., Yao S., Ai Y.-L., Feng X.-T., He Z.-Q., et al., 2023, *ApJS*, 265, 25. doi:10.3847/1538-4365/acaf89
- Kallivayalil N., van der Marel R. P., Alcock C., 2006, *ApJ*, 652, 1213. doi:10.1086/508014
- Kallivayalil N., van der Marel R. P., Besla G., Anderson J., Alcock C., 2013, *ApJ*, 764, 161. doi:10.1088/0004-637X/764/2/161
- Khan R., 2017, *ApJS*, 228, 5. doi:10.3847/1538-4365/228/1/5
- Lang, D. 2014, *AJ*, 147, 5, 108. doi:10.1088/0004-6256/147/5/108
- Liao S.-L., Qi Z.-X., Guo S.-F., Cao Z.-H., 2019, *RAA*, 19, 029. doi:10.1088/1674-4527/19/2/29
- Luo A.-L., Zhao Y.-H., Zhao G., et al., 2018, *yCat*, V/153
- Lyke, B. W., Higley, A. N., McLane, J. N., et al. 2020, *The Astrophysical Journal Supplement Series*, 250, 8. doi:10.3847/1538-4365/aba623.
- Mainieri, V., Anderson, R. L., Brinchmann, J., et al. 2024, , *The Wide-field Spectroscopic Telescope (WST) Science White Paper*, arXiv:2403.05398. doi:10.48550/arXiv.2403.05398
- Massey P., Olsen K. A. G., Hodge P. W., Strong S. B., Jacoby G. H., Schlingman W., Smith R. C., 2006, *AJ*, 131, 2478. doi:10.1086/503256
- Massey P., Neugent K. F., Smart B. M., 2016, *AJ*, 152, 62. doi:10.3847/0004-6256/152/3/62
- Massey P., Neugent K. F., Levesque E. M., 2019, *AJ*, 157, 227
- Mateos S., Alonso-Herrero A., Carrera F. J., Blain A., Watson M. G., Barcons X., Braitto V., et al., 2012, *MNRAS*, 426, 3271. doi:10.1111/j.1365-2966.2012.21843.x
- Meusinger H., Henze M., Birkle K., Pietsch W., Williams B., Hatzidimitriou D., Nesci R., et al., 2010, *A&A*, 512, A1. doi:10.1051/0004-6361/200913526
- Mishra S., Fox A. J., Krishnarao D., Lucchini S., D'Onghia E., Cashman F. H., Barger K. A., et al., 2024, *ApJL*, 976, L28. doi:10.3847/2041-8213/ad8b9d
- Morishita T., 2021, *ApJS*, 253, 4. doi:10.3847/1538-4365/abce67
- Nedialkov P., Williams B. F., Ivanov V. D., Valcheva A., 2018, *ATel*, 12250
- Neugent K. F., Massey P., Georgy C., 2012, *ApJ*, 759, 11. doi:10.1088/0004-637X/759/1/11
- Nilson P., 1973, *UGC...C*, 0
- Oke J. B., 1990, *AJ*, 99, 1621. doi:10.1086/115444
- Peters C. M., Richards G. T., Myers A. D., Strauss M. A., Schmidt K. B., Ivezić Ž., Ross N. P., et al., 2015, *ApJ*, 811, 95. doi:10.1088/0004-637X/811/2/95
- Peterson B. M., 1997, *iagn.book*
- Paiano S., Falomo R., Franceschini A., Treves A., Scarpa R., 2017, *ApJ*, 851, 135. doi:10.3847/1538-4357/aa9af4
- Rao S. M., Sardane G., Turnshek D. A., Thilker D., Walterbos R., Vanden Berk D., York D. G., 2013, *MNRAS*, 432, 866. doi:10.1093/mnras/stt417
- Richter, P., Fox, A. J., Wakker, B. P., et al. 2013, *ApJ*, 772, 2, 111. doi:10.1088/0004-637X/772/2/111
- Rusterucci S., Martin N. F., Starkenburg E., Ibata R., 2024, *A&A*, 692, A30. doi:10.1051/0004-6361/202452281
- Sarkisyan A. N., Vinokurov A. S., Solovieva Y. N., Sholukhova O. N., Kostenkov A. E., Fabrika S. N., 2017, *AstBu*, 72, 486. doi:10.1134/S1990341317040137
- Schlafly E. F., Finkbeiner D. P., 2011, *ApJ*, 737, 103. doi:10.1088/0004-637X/737/2/103
- Schlafly, E. F., Meisner, A. M., & Green, G. M. 2019, *ApJS*, 240, 2, 30. doi:10.3847/1538-4365/aafbea
- Skrutskie M. F., Cutri R. M., Stiening R., Weinberg M. D., Schneider S., Carpenter J. M., Beichman C., et al., 2006, *AJ*, 131, 1163. doi:10.1086/498708
- Storey-Fisher K., Hogg D. W., Rix H.-W., Eilers A.-C., Fabbian G., Blanton M. R., Alonso D., 2024, *ApJ*, 964, 69. doi:10.3847/1538-4357/ad1328
- Srianand R., Gupta N., Rahmani H., Momjian E., Petitjean P., Noterdaeme P., 2013, *MNRAS*, 428, 2198. doi:10.1093/mnras/sts190
- Tody D., 1993, *ASPC*, 52, 173
- Tody D., 1986, *SPIE*, 627, 733. doi:10.1117/12.968154
- van der Marel R. P., Fardal M. A., Sohn S. T., Patel E., Besla G., del Pino A., Sahlmann J., et al., 2019, *ApJ*, 872, 24. doi:10.3847/1538-4357/ab001b
- Vanden Berk D. E., Richards G. T., Bauer A., Strauss M. A., Schneider D. P., Heckman T. M., York D. G., et al., 2001, *AJ*, 122, 549. doi:10.1086/321167
- Warmels R. H., 1992, *ASPC*, 25, 115
- Walterbos R. A. M., Kennicutt R. C., 1987, *A&AS*, 69, 311
- Williams B. F., Hatzidimitriou D., Green J., Vasilopoulos G., Covarrubias R., Pietsch W. N., Stiele H., et al., 2014, *MNRAS*, 443, 2499. doi:10.1093/mnras/stu1252
- Williams B. F., Lang D., Dalcanton J. J., Dolphin A. E., Weisz D. R., Bell E. F., Bianchi L., et al., 2014, *ApJS*, 215, 9. doi:10.1088/0067-0049/215/1/9
- Worseck, G. & Prochaska, J. X. 2011, *ApJ*, 728, 1, 23. doi:10.1088/0004-637X/728/1/23
- Wright E. L., Eisenhardt P. R. M., Mainzer A. K., Ressler M. E., Cutri R. M., Jarrett T., Kirkpatrick J. D., et al., 2010, *AJ*, 140, 1868. doi:10.1088/0004-6256/140/6/1868
- York D. G., Khare P., Vanden Berk D., Kulkarni V. P., Crofts A. P. S., Lauroesch J. T., Richards G. T., et al., 2006, *MNRAS*, 367, 945. doi:10.1111/j.1365-2966.2005.10018.x

Table 2: Sample of 125 QSOs with redshifts based on optical spectrum, located within M31 isophote  $\mu_B=26^m/\square''$ . The position and the ID are from Gaia DR3 (Gaia Collaboration et al. 2023a), except for the objects marked with “*a*”; for them this information comes from Pan-STARRS Survey DR1 (Chambers et al. 2016). The distance  $\rho$  within the rectified plane of M31 is in fractions of the major isophotal radius  $\rho_{25}$ . The Class (name of best class) and the probability of the object being a quasar  $P_{QSO}$  (in %) from the Discrete Source Classifier-Combmode from Gaia DR3 (Gaia Collaboration et al. 2023b); when an object is missing a Class in there, we list its Class as “uncl” from unclassified, and if the object has no entry there, then the Class is set to “NA” from not applicable. References: (1) Gaia Collaboration et al. (2023a); (2) Storey-Fisher et al. (2024); (3) Dey et al. (2023); (4) Huo et al. (2013); (5) Neugent, Massey, & Georgy (2012); (6) this work; (7) Dong et al. (2018); (8) Liao et al. (2019); (9) Massey, Neugent, & Levesque (2019); (10) Dahari & De Robertis (1988); (11) Meusinger et al. (2010); (12) Dorn-Wallenstein, Levesque, & Ruan (2017); (13) Nedialkov et al. (2018); (14) Rao et al. (2013); (15) Paiano et al. (2017). Multiple references are given when we have reanalyzed spectra from the literature to remeasure the redshifts. Finally adopted redshift  $z_{adopt}$  is explained in Sect. 4.3. The analyzed original spectra are suffixed by A (Apache Point) or B (BTA) in the last column while the reanalyzed literature spectra are suffixed by M (Mayall) or L (LAMOST).

No	Gaia DR3 Name	RA DEC J2000	$\rho$	Gmag, mag	rms, mag	Class	P% QSO	$z_{lit}$	Ref.	Emis. lines	$z_{adopt}$	$A_V$ mag	Obs. log ID	Fig. 3 ID
1	380728681624635264	00:36:49.070 +40:08:41.73	1.161	18.921	0.078	uncl	100	0.502± 0.051	2		0.502± 0.051	0.000± 0.134		
2	380803551495086592	00:36:57.656 +40:25:50.28	1.228	19.311	0.095	AGN	97	1.181± 0.019 1.181± 0.074 1.208	1 2 3		1.208± 0.005	-0.262± 0.076		
3	380749950302728832	00:37:35.058 +40:09:41.68	0.997	18.682	0.114	AGN	100	0.337± 0.001 0.337± 0.085 0.335	1 2 4		0.337± 0.085	0.040± 0.129		
4	380736962321466240	00:37:50.796 +40:04:17.14	0.969	20.474	0.149	AGN	38	1.546± 0.018 1.264± 0.430	1 2		1.264± 0.430	0.057± 0.223		
5	368692465274338304	00:38:15.154 +39:42:23.99	1.184	20.010	0.145	uncl	1	1.038± 0.015 1.038± 0.143	1 2		1.038± 0.143	0.099± 0.111		
6	381143060069482496	00:38:40.836 +40:44:47.28	0.897	20.029	0.111	uncl	1	1.937± 0.032 0.710± 0.139	1 2		0.710± 0.139	0.290± 0.252		
7	381137287633113216	00:38:56.664 +40:34:46.56	0.745	20.330	0.143	uncl	87	2.851± 0.012 1.060± 0.209 2.867 2.760 2.868± 0.003	1 2 3 5 6;5		2.868± 0.003	0.305± 0.315		3856+4034M
8	381123371938862592	00:39:03.547 +40:28:52.68	0.708	20.396	0.145	uncl	100	5.191± 0.056 0.826± 0.133	1 2	Orv 1034, Or 1305, Crv 1400, Crv 1548, Crv 1909	0.826± 0.133	-0.530± 0.093		
9	380741944483858304	00:39:09.744 +40:14:01.98	0.782	20.251	0.194	uncl	36	2.762± 0.049 2.762± 0.274	1 2		2.762± 0.274	0.577± 0.343		
10	380741742621118464	00:39:11.005 +40:13:02.05	0.782	19.478	0.136	AGN	99	2.552± 0.050 2.552± 0.096	1 2		2.552± 0.096	-0.010± 0.144		
11	381143850343346304	00:39:14.123 +40:40:42.74	0.701	20.321	0.152	AGN	20	0.606± 0.013 0.915± 0.532	1 2		0.915± 0.532	1.173± 0.173		
12	368731360498431104	00:39:16.399 +40:08:21.33	0.850	18.825	0.097	AGN	100	1.935± 0.013 1.935± 0.098	1 2		1.935± 0.098	0.073± 0.069		
13	368731158635535232	00:39:16.942 +40:06:21.77	0.878	20.497	0.197	CEP	99	0.099± 0.012 1.025± 0.190	1 2		1.025± 0.190	0.445± 0.261		

Table 2: Continued.

No	Gaia DR3 Name	RA DEC J2000	$\rho$	Gmag, mag	rms, mag	Class	P% QSO	$z_{lit}$	Ref.	Emis. lines	$z_{adopt}$	$A_V$ mag	Obs. log ID	Fig. 3 ID
14	368728508640097792	00:39:17.049 +40:01:06.97	0.957	20.328	0.173	AGN	100	2.046± 0.016 2.046± 0.074	1 2		2.046± 0.074	0.228± 0.226		
15	381231021002898048	00:39:21.921 +41:20:31.31	1.219	20.525	0.277	AGN	100	4.619± 0.042 1.425± 0.005	1 6		1.425± 0.005	-0.644± 0.347	1	3921+4120B
16	381230200663395712	00:39:28.105 +41:19:13.09	1.160	20.765	0.224	AGN	69	2.029± 0.025 2.057± 0.001	1 6	CIII] 1909, MgII 2799	2.057± 0.001	-0.176± 0.181	2	3928+4119B
17	381226451157559040	00:39:30.165 +41:13:44.06	1.050	19.754	0.124	AGN	100	2.656± 0.023 2.656± 0.408	1 2		2.656± 0.408	0.143± 0.180		
18	381223637953333376	00:39:34.595 +41:07:38.52	0.920	19.876	0.187	AGN	100	0.101± 0.008 1.570± 0.001	1 6		1.570± 0.001	0.525± 0.103	3	3934+4107B
19	381225214206911488	00:39:34.908 +41:09:34.67	0.951	19.874	0.142	AGN	69	0.683± 0.004 0.681± 0.140 0.673	1 2 3		0.673± 0.005	1.228± 0.231		
20	381236346762388352	00:39:41.636 +41:23:27.88	1.164	19.244	0.128	AGN	99	1.346± 0.018 1.346± 0.102	1 2		1.346± 0.102	0.241± 0.106		
21	381251297542795904	00:39:47.423 +41:31:47.53	1.293	20.313	0.397	AGN	100	0.650± 0.008 0.794± 0.244 1.208 0.6535± 0.0003	1 2 3 6		0.6535± 0.0003	-0.172± 0.109	4	3947+4131B
22	381236900812096128	00:39:51.346 +41:25:43.70	1.153	19.982	0.139	AGN	100	1.505± 0.013 1.505± 0.081 1.484 1.489± 0.006	1 2 8 6;8		1.489± 0.006	0.376± 0.166		3951+4125L
23	369106710576624000	00:39:52.606 +40:13:07.43	0.808	19.789	0.156	AGN	100	1.258± 0.022 1.199± 0.224	1 2		1.199± 0.224	0.341± 0.084		
24	369102106371697792	00:40:08.957 +40:06:18.11	0.958	19.878	0.115	AGN	100	2.205± 0.012 2.205± 0.056 2.197	1 2 3		2.197± 0.005	-0.027± 0.062		
25	368710061756016896	00:40:18.510 +39:53:56.24	1.229	19.760	0.148	AGN	100	0.286± 0.002 0.344± 0.081 0.284 0.280 0.282 0.2845± 0.0002	1 2 3 7 8 6;8		0.2845± 0.0002	-0.319± 0.067		4018+3953L
26	381129870225085056	00:40:24.120 +40:39:34.61	0.475	20.207	0.160	uncl	100	2.347± 0.025 1.209± 0.282	1 2		1.209± 0.282	0.358± 0.224		

Table 2: Continued.

No	Gaia DR3 Name	RA DEC J2000	$\rho$	Gmag, mag	rms, mag	Class	P% QSO	$z_{lit}$	Ref.	Emiss. lines	$z_{adopt}$	$A_V$ mag	Obs. log ID	Fig. 3 ID
27	381129011231416704	00:40:29.727 +40:37:05.68	0.491	18.986	0.076	NA	-	1.585± 0.007	6	Siv 1400 CIII] 1909, MgII 2799	1.585± 0.007	0.521± 0.077	6	4029+4037A
28	381172953042364032	00:40:32.571 +41:00:43.81	0.500	20.001	0.144	AGN	15	0.358± 0.011 0.845± 0.220	1 2		0.845± 0.220	1.216± 0.201		
29	381130007666198272	00:40:32.954 +40:41:02.66	0.451	19.451	0.092	uncl	38	4.347± 0.009 0.944± 0.180	1 2		0.944± 0.180	0.230± 0.390		
30	369089496347724160	00:40:35.038 +40:03:45.04	1.080	19.951	0.125	AGN	74	1.345± 0.016 1.463± 0.368	1 2		1.463± 0.368	0.105± 0.133		
31	381335955644522880	00:40:38.203 +41:40:59.97	1.202	19.883	0.143	uncl	100	1.783± 0.014 1.783± 0.112	1 2		1.783± 0.112	0.213± 0.145		
32	369112409997076224	00:40:42.592 +40:22:16.27	1.202	19.690	0.132	AGN	100	3.542± 0.041 0.972± 0.065	1 2		0.972± 0.065	0.179± 0.043		
33	381180615264154496	00:40:43.101 +41:08:45.81	0.555	17.963	0.081	uncl	86	4.342± 0.001 0.920± 0.095	1 2		0.920± 0.095	0.486± 1.005		
34	369086021717454208	00:40:43.463 +39:59:04.35	1.205	20.455	0.212	AGN	100	1.387± 0.026 1.387± 0.213	1 2		1.387± 0.213	-0.373± 0.194		
35	381330011408893312	00:40:52.613 +41:32:27.82	0.947	19.348	0.138	AGN	100	0.327± 0.006 0.974± 0.264	1 2		0.974± 0.264	-0.180± 0.199		
36	369111486580379648	00:40:52.617 +40:21:02.41	0.785	19.429	0.083	uncl	57	2.902± 0.017 2.902± 0.444	1 2		2.902± 0.444	0.194± 0.139		
37	381342621433074688	00:40:55.554 +41:47:46.01	1.251	19.479	0.121	AGN	100	1.473± 0.028 2.156± 0.751	1 2		2.156± 0.751	0.486± 0.239		
38	369087915799918976	00:41:07.984 +40:02:48.52	1.214	19.917	0.137	AGN	100	1.612± 0.016 1.612± 0.097 1.615 1.621 1.615± 0.001	1 2 7 8 6;8		1.615± 0.001	0.055± 0.073		4107+4002L
39	381166360266825216	00:41:15.366 +41:01:02.64	0.294	19.557	0.111	uncl	55	1.423± 0.017 0.946± 0.232	1 2		0.946± 0.232	0.302± 0.228		
40	381331213997851136	00:41:24.304 +41:36:49.65	0.866	20.442	0.188	AGN	100	1.612± 0.033 1.612± 0.263	1 2		1.612± 0.263	0.377± 0.079		
41	381161584267072896	00:41:26.217 +40:53:26.55	0.285	19.957	0.209	NA	-	1.159 1.157 1.157± 0.003 1.155± 0.008	3 9 6;9 6		1.155± 0.008	0.319± 0.147		4126+4053M 8 4126+4053A
42	381169864962593536	00:41:27.909 +41:12:18.55	0.363	19.372	0.076	uncl	43	0.507± 0.014	1	CIII] 1909, MgII 2799	0.628± 0.059	-0.184± 0.267		

Table 2: Continued.

No	Gaia DR3 Name	RA DEC J2000	$\rho$	Gmag, mag	rms, mag	Class	P% QSO	$z_{lit}$	Ref.	Emis. lines	$z_{adopt}$	$A_V$ mag	Obs. log ID	Fig. 3 ID
								0.628± 0.059	2					
43	381277544086058880	00:41:30.240 +41:23:20.22	0.555	19.505	0.085	NA	-	1.895	9		1.900± 0.011	1.768± 0.246		4130+4123M
								1.900± 0.011	6;9	C III] 1909				
44	381341251346342016	00:41:36.120 +41:52:29.22	1.141	20.291	0.226	uncl	69	1.192± 0.024	1		1.192± 0.607	0.537± 0.119		
								1.192± 0.607	2					
45	381164710999391104	00:41:37.918 +41:01:07.82	0.213	19.404	0.091	uncl	79	1.450	5		1.466± 0.002	0.445± 0.154		4137+4101M
								1.465± 0.004	6;5	C IV 1548, C III] 1909, Mg II 2799			9	4137+4101A
								1.466± 0.002	6	C IV 1548, C III] 1909, Mg II 2799, O II 3727				
46	381276410213544064	00:41:41.408 +41:19:16.85	0.413	18.569	0.069	uncl	28	1.238± 0.014	1		1.243± 0.039	0.572± 0.162		
								1.220± 0.159	2					
								1.264	3					
								1.245	9					
								1.246± 0.015	6;9	C III] 1909, Mg II 2799				4141+4119M
								1.243± 0.039	6	C III] 1909, Mg II 2799			10	4141+4119A
47	369137599981515648	00:41:41.489 +40:31:17.91	0.729	18.603	0.101	AGN	100	2.165± 0.008	1		2.146± 0.006	0.717± 0.230		
								2.165± 0.100	2					
								2.151	9					
								2.146± 0.006	6;9	S IV+O IV] 1399, C IV 1548				4141+4031M
48	381279575604763264	00:41:45.168 +41:26:23.58	0.535	20.121	0.135	uncl	92	1.311± 0.017	1		1.293± 0.003	0.315± 0.234		4145+4126M
								1.297	3					
								1.293	9					
								1.293± 0.003	6;9	C III] 1909, Mg II 2799				
49	381165260757784192	00:41:47.512 +41:03:51.75	0.181	19.847	0.127	uncl	42	0.984± 0.017	1		0.839± 0.107	0.997± 0.205		
								0.839± 0.107	2					
50	369125604136776832	00:41:49.837 +40:28:18.01	0.825	19.522	0.103	AGN	0	1.230	4		1.230± 0.002	0.743± 0.094		
51	381340284969411712	00:41:57.224 +41:50:48.36	0.998	20.084	0.144	uncl	100	0.395± 0.021	1		1.211± 0.241	-0.109± 0.101		
								1.211± 0.241	2					
52	369124229747134464	00:42:04.572 +40:24:05.28	0.977	20.215	0.142	AGN	100	1.415± 0.019	1		0.931± 0.341	-0.267± 0.131		
								0.931± 0.341	2					
53	381364199347501696	00:42:09.323 +41:55:38.33	1.044	20.200	0.121	AGN	52	0.855± 0.018	1		0.855± 0.103	0.209± 0.166		
								0.855± 0.103	2					
54	369128009318757120	00:42:11.127 +40:36:53.38	0.724	20.237	0.163	AGN	100	1.617± 0.031	1		1.617± 0.111	0.022± 0.106		
								1.617± 0.111	2					
55	369145670224353664	00:42:14.124 +40:39:20.52	0.683	18.770	0.147	AGN	90	0.775± 0.007	1		0.7579± 0.0007	0.396± 0.110		
								0.775± 0.354	2					
								0.757	8					

Table 2: Continued.

No	Gaia DR3 Name	RA DEC J2000	$\rho$	Gmag, mag	rms, mag	Class	P% QSO	$z_{lit}$	Ref.	Emis. lines	$z_{adopt}$	$A_v$ mag	Obs. log ID	Fig. 3 ID
								0.7579± 6;8 0.0007		MgII 2799, OII 3727, H $\beta$ 4863, OIII 4959&5007				4214.1+4039L
56	369145773303561856	00:42:14.991 +40:39:09.54	0.690	19.874	0.113	AGN	46	1.780± 0.010	1		1.778± 0.001	0.079± 0.034		
								1.774 1.778± 6;9 0.001	9	CIV 1548, CIII] 1909				4214+4039M
57	381266244030810880	00:42:15.487 +41:20:31.52	0.249	20.549	0.156	NA	-	1.520± 0.020	6	CIV 1548, CIII] 1909, MgII 2799	1.520± 0.020	0.259± 0.400	11	4215+4120A
58	369120145234465024	00:42:16.121 +40:19:35.88	1.127	16.852	0.326	AGN	100	0.101± 0.001	1		0.1029± 0.0002	0.838± 0.425		
								0.116± 2 0.056 0.103 10 0.102 8 0.1029± 6;8 0.0002	2 10 8	OII 3727, H $\beta$ 4863, H $\gamma$ 4340, OIII 4959&5007, H $\alpha$ 6565				4216+4019L
59	369152821344393344	00:42:24.770 +40:53:53.80	0.407	20.281	0.120	uncl	100	0.524± 0.017	1		0.777± 0.087	-0.343± 0.004		
								0.777± 2 0.087	2					
60	381287714569113600	00:42:30.291 +41:36:59.33	0.530	20.616	0.143	NA		1.667	3		1.667± 0.005	1.326± 0.225		
61	381318951872849152	00:42:31.788 +41:55:48.32	0.939	20.029	0.124	AGN	84	1.258± 0.024	1		1.246± 0.135	0.331± 0.159		
								1.246± 2 0.135	2					
62	369148728241389056	00:42:35.002 +40:48:39.20	0.567	18.811	0.131	uncl	100	0.728± 0.005	1		0.725± 0.002	-0.171± 0.242		
								0.728± 2 0.083 0.725± 6 0.002	2 6	MgII 2799, NVI 3426, OII 3727, H $\delta$ , 4102, H $\gamma$ 4340, H $\beta$ 4863, OIII 4959&5007			12	4235+4048A
63	369072758858914304	00:42:38.628 +40:17:43.04	1.271	20.074	0.109	uncl	26	2.215± 0.029	1		2.215± 0.065	-0.022± 0.040		
								2.215± 2 0.065	2					
64	381274864026764672	00:42:42.235 +41:32:40.02	0.377	19.221	0.083	uncl	7	3.738± 0.048	1		0.916± 0.088	0.001± 0.541		
								0.916± 2 0.088	2					
65	381324342051592832	00:42:42.912 +41:59:46.78	0.976	20.393	0.137	uncl	51	0.524± 0.012	1		1.084± 0.005	-0.070± 0.202		
								1.110± 2 0.393 1.084 3	2 3					
66	369230504420183808	00:43:07.665 +40:48:39.61	0.722	20.422	0.146	AGN	20	0.520± 0.016	1		0.663± 0.206	0.9252± 0.251		
								0.663± 2 0.206	2					
67	369081761110670464	00:43:18.274 +40:29:26.57	1.200	20.072	0.123	AGN	3	0.375± 0.012	1		0.686± 0.151	1.015± 0.372		
								0.686± 2 0.151	2					
68	369259130379725056	00:43:30.232 +41:19:02.43	0.207	17.561	0.062	uncl	91	0.087± 0.0004	1		0.821± 0.457	-0.228± 0.248		
								0.821± 2 0.457	2					
69	381322417905768448	00:43:38.492 +42:00:59.49	0.768	20.378	0.125	uncl	100	0.560± 0.010	1		1.469± 0.500	-0.311± 0.413		
								1.469± 2 0.500	2					



Table 2: Continued.

No	Gaia DR3 Name	RA DEC J2000	$\rho$	Gmag, mag	rms, mag	Class	P% QSO	$z_{lit}$	Ref.	Emis. lines	$z_{adopt}$	$A_V$ mag	Obs. log ID	Fig. 3 ID
85	387349012934217856	00:45:01.357 +42:28:07.73	1.068	20.333	0.144	AGN	2	1.680± 0.017	1		2.588± 0.743	1.061± 0.249		
								2.588± 0.743	2					
86	369212809151892224	00:45:11.917 +41:00:04.05	1.141	19.109	0.095	AGN	98	1.125± 0.016	1		1.125± 0.080	-0.059± 0.115		
								1.125± 0.080	2					
								1.144	4					
87	387355232046935808	00:45:16.119 +42:31:38.89	1.098	20.063	0.121	AGN	53	1.587± 0.019	1		1.596± 0.005	0.053± 0.034		
								1.587± 0.051	2					
								1.596	3					
88	369188138866012928	00:45:18.192 +40:54:32.72	1.290	19.299	0.082	uncl	99	0.237± 0.013	1		1.227± 0.005	0.123± 0.097		
								1.081± 0.144	2					
								1.227	3					
								1.228	4					
89	375300289639502464	00:45:22.568 +41:50:34.60	0.499	18.343	0.062	uncl	100	4.356± 0.005	1		0.939± 0.062	-0.387± 0.201		
								0.939± 0.062	2					
90	375308432897586560	00:45:26.694 +41:59:16.06	0.554	18.674	0.068	uncl	100	4.376± 0.037	1		0.998± 0.193	-0.611± 0.193		
								0.998± 0.193	2					
91	387347093084980992	00:45:26.934 +42:20:38.44	0.861	19.904	0.101	uncl	3	2.928± 0.017	1		2.928± 0.171	0.133± 0.077		
								2.928± 0.171	2					
92	369288714109887744	00:45:27.311 +41:32:54.09	0.637	20.387	0.271	uncl	3	1.129± 0.008	1		0.209± 0.001	1.984± 0.583		
								0.215	12					
								0.209± 0.001	6	H $\alpha$ 6565			23	4527+4132A
93	369276756923364224	00:45:28.249 +41:29:43.92	0.687	19.536	0.119	uncl	22	0.201± 0.003	1		0.2035± 0.0008	0.038± 0.120		
								0.203	13					
								0.2035± 0.0008	6	OII 3727, H $\beta$ 4863, OIII 4959& 5007, H $\alpha$ 6565			24	4528+4129A
94	369270945831405184	00:45:42.149 +41:23:59.30	0.855	20.182	0.121	uncl	3	4.846± 0.058	1		1.365± 0.207	0.410± 0.066		
								1.365± 0.207	2					
95	369270469091280000	00:45:43.426 +41:20:30.86	0.922	19.267	0.106	AGN	98	1.317± 0.011	1		1.320± 0.006	-0.069± 0.117		
								1.323	9					
								1.322± 0.003	6;9	CIII] 1909, MgII 2799				4543+4120M
								1.320± 0.006	6	CIV 1548, CIII] 1909, MgII 2799			25	4543+4120A
96	369276138450478336	00:45:56.459 +41:31:01.15	0.820	20.001	0.136	AGN	100	0.234± 0.009	1		2.064± 0.492	-0.092± 0.398		
								2.064± 0.492	2					
97	375343552846494080	00:45:59.021 +42:26:55.96	0.920	19.952	0.191	AGN	100	1.815± 0.018	1		1.815± 0.127	-0.277± 0.213		
								1.815± 0.127	2					
98	375343346688063104	00:46:03.457 +42:24:06.46	0.869	20.157	0.223	uncl	94	2.509± 0.022	1		2.509± 0.377	0.462± 0.174		
								2.509± 0.377	2					

Table 2: Continued.

No	Gaia DR3 Name	RA DEC J2000	$\rho$	Gmag, mag	rms, mag	Class	P% QSO	$z_{lit}$	Ref.	Emis. lines	$z_{adopt}$	$A_V$ mag	Obs. log ID	Fig. 3 ID
99	369271740398774784	00:46:15.916 +41:24:14.62	1.037	19.789	0.142	AGN	100	0.946± 0.011 0.946± 0.053	1 2		0.946± 0.053	-0.352± 0.044		
100	375284415439911296	00:46:16.832 +41:43:00.73	0.767	20.479	0.156	uncl	69	5.883± 0.057 0.974± 0.246	1 2		0.974± 0.246	0.272± 0.211		
101	375332759593218432	00:46:21.066 +42:13:08.00	0.734	17.846	0.076	uncl	100	4.350± 0.004 0.920± 0.053	1 2		0.920± 0.053	-0.032± 0.213		
102	375436285483408128	00:46:22.493 +42:30:55.18	0.958	20.335	0.196	uncl	72	0.510± 0.011 0.671± 0.144	1 2		0.671± 0.144	0.761± 0.187		
103	375439931911909504	00:46:23.449 +42:35:59.76	1.039	20.107	0.148	AGN	100	1.359± 0.013 1.359± 0.293	1 2		1.359± 0.293	0.103± 0.087		
104	375332523368128128	00:46:30.765 +42:13:46.81	0.751	18.677	0.062	uncl	100	1.002± 0.013 1.950± 0.561	1 2		1.950± 0.561	-0.385± 0.176		
105	375448173953465728	00:46:31.175 +42:44:38.46	1.178	19.353	0.229	AGN	100	0.874± 0.007 0.874± 0.077	1 2		0.874± 0.077	0.700± 0.511		
106	375277577851726848	00:46:33.154 +41:33:05.80	0.987	19.457	0.094	uncl	3	3.014± 0.054 0.956± 0.607	1 2		0.956± 0.607	0.764± 0.135		
107	375317503869019776	00:46:41.844 +42:00:28.87	0.751	18.337	0.069	uncl	19	1.353± 0.015 1.378± 0.260	1 2		1.378± 0.260	0.018± 0.062		
108	375328709439174400	00:46:55.515 +42:20:50.09	0.839	17.648	0.137	AGN	100	0.308± 0.001 0.308± 0.060 0.310 0.307 0.3078± 0.0007 0.3065± 0.0005	1 2 14 8 6;8 6		0.3065± 0.0007	-0.281± 0.139		4655 +4220L 27 4655+4220A
109	375328395906539392	00:47:02.870 +42:18:37.19	0.835	19.902	0.103	uncl	10	2.419± 0.016 1.088± 0.188 0.626± 0.011	1 2 6		0.626± 0.011	0.444± 0.160		28 4702+4218A
110	375444428741949184	00:47:08.606 +42:43:02.42	1.105	20.149	0.343	uncl	97	0.847± 0.025 2.048± 0.219	1 2		2.048± 0.219	0.264± 0.138		
111	375328876942905472	00:47:13.476 +42:20:47.66	0.867	19.923	0.132	AGN	59	1.240± 0.018 1.240± 0.533 1.226± 0.003	1 2 6		1.226± 0.003	0.368± 0.184		29 4713+4220A
112	375285927268328064	00:47:15.941 +41:40:47.86	1.102	19.973	0.211	AGN	100	1.553± 0.009 1.553± 0.089	1 2		1.553± 0.089	-0.663± 0.095		

Table 2: Continued.

No	Gaia DR3 Name	RA DEC J2000	$\rho$	Gmag, mag	rms, mag	Class	P% QSO	$z_{lit}$	Ref.	Emis. lines	$z_{adopt}$	$A_V$ mag	Obs. log ID	Fig. 3 ID
113	375313213198402432	00:47:18.499 +41:55:44.21	0.936	19.723	0.113	AGN	8	0.752± 0.021 1.806± 0.509	1 2		1.806± 0.509	0.278± 0.246		
114	375423920274397824	00:47:35.750 +42:25:49.99	0.937	20.402	0.189	uncl	71	5.052± 0.057 1.564± 0.274	1 2		1.564± 0.274	0.001± 0.209		
115	375423881617811328	00:47:39.120 +42:26:17.76	0.945	18.197	0.065	AGN	100	2.880± 0.026 0.850± 0.147 0.705± 0.001	1 2 6		0.705± 0.001	0.171± 0.136	30	4739+4226A
116	375322314232658048	00:47:42.847 +42:10:16.93	0.945	19.738	0.109	AGN	87	1.470± 0.020 1.450 1.448± 0.003	1 5 6;5		1.445± 0.004	0.234± 0.094		4742+4210M
													31	4742+4210A
117	375457691601073792	00:47:48.288 +42:49:03.13	1.173	19.206	0.093	AGN	90	0.988± 0.012 0.988± 0.079	1 2		0.988± 0.079	-0.208± 0.061		
118	375418590218050304	00:47:48.323 +42:19:34.31	0.949	19.128	0.099	AGN	4	0.341± 0.003 0.798± 0.328 0.769± 0.002	1 2 6		0.769± 0.002	0.550± 0.199	32	4748+4219A
119	375427558110226816	00:47:55.077 +42:31:18.97	1.003	20.238	0.141	AGN	24	1.233± 0.015 1.455± 0.288	1 2		1.455± 0.288	0.636± 0.118		
120	375417971742745984	00:48:15.473 +42:18:00.79	1.040	20.402	0.223	AGN	100	2.547± 0.037 0.967± 0.231	1 2		0.967± 0.231	0.184± 0.424		
121	375453332209648256	00:48:22.580 +42:42:13.67	1.120	19.943	0.131	AGN	99	1.527± 0.019 1.527± 0.081 1.516	1 2 3		1.516± 0.005	-0.008± 0.088		
122	158740121024692127 <sup>a</sup>	00:48:24.598 +42:17:04.18	1.078	22.129	0.181	NA	-	0.293 0.292± 0.002	8 6;8		0.292± 0.002	1.028± 0.574		4824+4217L
123	375405499158263168	00:48:35.085 +42:36:31.52	1.109	20.065	0.154	AGN	100	1.908± 0.021 0.774± 0.464	1 2		0.774± 0.464	0.225± 0.227		
124	375378320605062144	00:48:59.160 +42:23:51.06	1.182	19.525	0.347	AGN	1	2.928± 0.051 0.724± 1.326 0.302	1 2 15			-9.999± -9.999		
125	375404197783072128	00:49:09.622 +42:33:18.28	1.197	20.316	0.183	AGN	3	0.145± 0.011 1.984± 0.477	1 2		1.984± 0.477	1.488± 0.181		

## Appendix A: Data availability

Table A.1 lists the spectra that are reported for the first time in this paper.

Table A.1: New spectra, reported here for the first time. Only part of the table is shown as an example. The entire table is available only in electronic form at the CDS.

$\lambda$ [Angström]	Flux [arbitrary units]
J004029.727+403705.68	
3533	1.104
3535	1.222
3537	0.995
3538	1.229
3540	1.041
3542	0.960
3544	1.293
...	
J004215.487+412031.52	
3801	0.429
3803	1.196
3805	1.275
3807	1.742
3809	0.767
3811	1.595
3813	2.027
...	

## Appendix B: Intrinsic colors of quasars

Table B.1 lists the derived intrinsic colors of quasars, as shown with black lines in Fig. 5.

Table B.1: Intrinsic colors of quasars. N is the number of quasars in the respective redshift  $z$  bin (bin size 0.2 dex); the numbers of some colors can be smaller if there are quasars with missing photometry.

$z$	$(g-r)$ [mag]	$(g-i)$ [mag]	$(g-z)$ [mag]	$(g-y)$ [mag]	N
0.1	0.222±0.151	0.569±0.258	0.586±0.239	0.697±0.286	8
0.3	0.266±0.201	0.408±0.305	0.800±0.264	0.612±0.402	79
0.5	0.062±0.168	0.312±0.258	0.297±0.321	0.694±0.272	138
0.7	0.061±0.120	0.138±0.213	0.254±0.224	0.251±0.298	187
0.9	0.118±0.163	0.118±0.235	0.190±0.251	0.306±0.294	249
1.1	0.250±0.118	0.229±0.173	0.159±0.193	0.319±0.223	273
1.3	0.262±0.124	0.287±0.182	0.257±0.193	0.314±0.197	270
1.5	0.193±0.130	0.349±0.160	0.327±0.167	0.339±0.216	295
1.7	0.081±0.116	0.301±0.174	0.286±0.160	0.329±0.210	262
1.9	0.078±0.119	0.260±0.148	0.337±0.174	0.392±0.196	222
2.1	0.092±0.111	0.178±0.162	0.357±0.179	0.367±0.197	173
2.3	0.076±0.116	0.151±0.145	0.325±0.177	0.442±0.171	174
2.5	0.080±0.121	0.123±0.162	0.235±0.157	0.440±0.164	124
2.7	0.136±0.134	0.213±0.178	0.280±0.161	0.434±0.223	94
2.9	0.119±0.119	0.225±0.163	0.204±0.165	0.377±0.131	62
3.1	0.248±0.085	0.361±0.223	0.306±0.201	0.467±0.160	34

## Appendix C: Correction of the *Spitzer* coordinates

The coordinate accuracy of candidate quasars is crucial for their cross-identification for the optical spectroscopic follow up. Most of our candidates are selected on the base of their *Spitzer* photometry (Khan 2017), but a comparison with various near-infrared and optical catalogs revealed systematic offsets in this coordinate system. Therefore, we decided to transfer

the *Spitzer* coordinates of Khan (2017) to the *WISE* J2000 coordinate system. We cross-matched the *Spitzer* and *WISE* coordinates with 3'' matching radius, for objects with  $[W2] \leq 13.5$  mag and  $-0.35 \text{ mag} \leq [W2] - [W1] \leq 0.35$  mag as shown in Fig. 2 (top right panel), to ensure we only consider high signal-to-noise detections and to reduce the number of spurious matches. Then, we formed the *Spitzer*–*WISE* coordinate differences  $\delta RA$  and  $\delta DEC$ , for these sources, plotted them versus each other (Fig.C.1, top left) and saw a two-clump structure. We imposed an initial separation between the two clumps along the blue line. The objects above and below it (plotted everywhere with black and red dots, respectively) are located into two distinct spatial regions on the sky, separated with a line connecting the following positions in RA, DEC (J2000), in degrees: (9.714, 41.195), (10.140, 41.048), (10.963, 41.874), (11.685, 41.874), (11.920, 42.010) and (12.186, 42.005) – marked with green solid line in Fig. C.2. For all objects within each of these two areas we derived separately polynomial fits, with 3- $\sigma$  clipping, of  $\delta RA$  and  $\delta DEC$  versus DEC and RA, respectively (Fig.C.1, middle and lower panels), based on about 1600 objects in total:

$$\delta DEC_{black} = -1.671 + 0.36211 \times RA - 0.014715 \times RA^2 \quad (C.1)$$

$$\delta DEC_{red} = -405.401 + 107.03023 \times RA - 9.006573 \times RA^2 + 0.2022619 \times RA^3 + 0.00327904 \times RA^4 \quad (C.2)$$

$$\delta RA_{black} = -26974.840 + 1920.434447 \times DEC - 45.5512001 \times DEC^2 + 0.35995935 \times DEC^3 \quad (C.3)$$

$$\delta RA_{red} = 8571.288 - 620.935448 \times DEC + 15.0056471 \times DEC^2 - 0.12096752 \times DEC^3 \quad (C.4)$$

The typical RMS of these relations is  $\sim 0.3''$ . Applying them brings the two clumps together (Fig.C.1, upper right panel).

A minor caveat in this correction is the omission of the proper motions of the brightest sources that are probably Milky Way stars, but the Gaia DR3 suggests there are of order of 10–20 mas yr<sup>-1</sup>. Fortunately, the *Spitzer*–*WISE* time baseline is  $\sim 5$  yr, so any cumulative effect from the proper motions can safely be neglected.

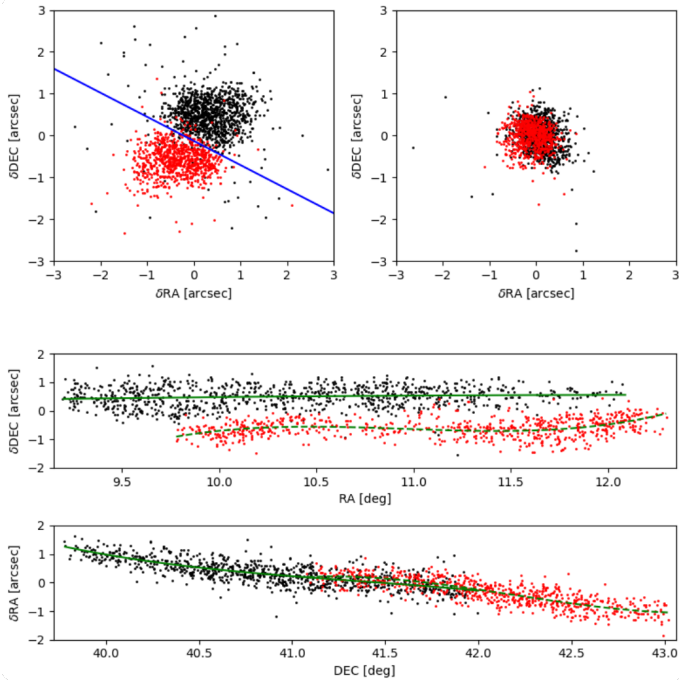


Fig. C.1: Upper left:  $\delta RA/\delta DEC$  plot for the astrometric *Spitzer–WISE* comparison of 1623 objects from our bright astrometric sample. The double central clump is due to small systematic deviations in the Khan (2017) coordinate system. The blue line makes initial division of the astrometric sample into two spatially distinct sub-samples of  $\sim 700$  and  $\sim 900$  objects (see Fig. C.2). Upper right: the same plot after  $3\sigma$  clipping and correcting for the systematic effect to the WISE coordinate system. Middle:  $\delta DEC(\textit{Spitzer–WISE})$  versus *WISE* RA. Bottom:  $\delta RA(\textit{Spitzer–WISE})$  versus *WISE* DEC. The solid and dashed green curves are the best fits to the trends for the two sub-samples on the middle and bottom panels (see text).

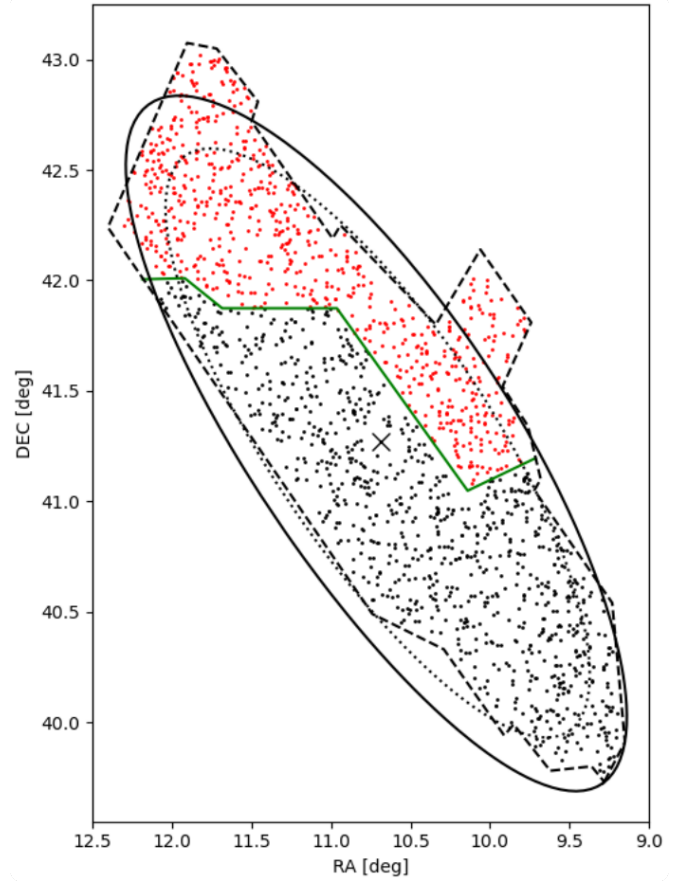


Fig. C.2: Map of our astrometric sample of 1623 objects with the adopted final dividing solid line (solid green) for the two spatially distinct samples of 710 (red dots) and 913 (black dots) objects. The dashed line shows the approximate outline of Khan (2017) catalog, the solid and dotted lines show the  $\mu_B=26^m/\square''$  and  $\mu_B=25^m/\square''$  isophotes, respectively. M 31 center is marked with an x.